

Dependence of Red Blood Cell Dynamics in Microvessel Bifurcations on the Endothelial Surface Layer's Resistance to Flow and Compression

Carlson Triebold^{1,2} · Jared Barber^{*,1,3}

Received: date / Accepted: date

Abstract Red blood cells (RBCs) make up 40-45% of blood and play an important role in oxygen transport. That transport depends on the RBC distribution throughout the body, which is highly heterogeneous. That distribution, in turn, depends on how RBCs are distributed or partitioned at diverging vessel bifurcations where blood flows from one vessel into two. Several studies have used mathematical modeling to consider RBC partitioning at such bifurcations in order to produce useful insights. These studies, however, assume that the vessel wall is a flat impenetrable homogeneous surface. While this is a good first approximation, especially for larger vessels, the vessel wall is typically coated by a flexible, porous endothelial glycocalyx or endothelial surface layer (ESL) that is on the order of 0.5-1 μm thick. To better understand the possible effects of this layer on RBC partitioning, a diverging capillary bifurcation is analyzed using a flexible, two-dimensional model. In addition, the model is also used to investigate RBC deformation and RBC penetration of the ESL region when ESL properties are varied. The RBC is represented using interconnected viscoelastic elements. Stokes flow equations (viscous flow) model the surrounding fluid. The flow in the ESL is modeled using the Brinkman approximation for porous media with a corresponding hydraulic resistivity. The ESL's resistance to compression is modeled using an osmotic pressure. One cell passes through the bifurcation at a time so there are no cell-cell interactions. A range of physiologically relevant hydraulic resistivities and osmotic pressure differences are explored. Decreasing hy-

draulic resistivity and/or decreasing osmotic pressure differences (ESL resistance to compression) produced four behaviors: 1) RBC partitioning nonuniformity increased slightly; 2) RBC deformation decreased; 3) RBC velocity decreased relative to blood flow velocity; and 4) RBCs penetrated more deeply into the ESL. Decreasing the ESL's resistance to flow and/or compression to pathological levels could lead to more frequent cell adhesion and clotting as well as impaired vascular regulation due to weaker ATP and nitric oxide release. Potential mechanisms that can contribute to these behaviors are also discussed.

Keywords Microvessel · Bifurcation · Endothelial surface layer · Red blood cell mechanics · Capillary flow

Declarations

Funding: Department of Mathematics in the School of Science at IUPUI Startup Funds; NSF grant DMS-1522554 (software purchase).

Conflicts of interest/Competing interests: None.

Availability of data and material: Available upon request.

Code availability: Available upon request.

Author's contributions: Both authors contributed to the conception and design of the study. Triebold ran all simulations, adapted the model to include the ESL and consider RBCs in bifurcations, analyzed results, and wrote the initial manuscript and carried out successive edits. Barber supervised the project, constructed early versions of the model, assisted with analysis, and oversaw, reviewed, and edited the paper.

*Corresponding Author

¹Indiana University - Purdue University Indianapolis, Department of Mathematical Sciences

²E-mail: cbtriebo@iu.edu; ORCID: 0000-0001-8694-0148

³E-mail: jarobarb@iu.edu; ORCID: 0000-0002-8414-6642

This is the author's manuscript of the article published in final edited form as:

Triebold, C., & Barber, J. (2022). Dependence of red blood cell dynamics in microvessel bifurcations on the endothelial surface layer's resistance to flow and compression. *Biomechanics and Modeling in Mechanobiology*, 21(3), 771–796. <https://doi.org/10.1007/s10237-022-01560-x>

1 Introduction

This study focuses on two key players in blood flow dynamics, red blood cell (RBC) partitioning and the endothelial surface layer (ESL). At diverging vessel bifurcations where blood flows from one mother vessel into two daughter vessels, RBCs are often partitioned nonuniformly where, for instance, 5% of the RBCs go into one daughter branch even though 25% of the total blood flow goes into that branch (Schmid-Schonbein et al., 1980; Pries and Secomb, 2005). This contributes to the heterogeneous microvascular RBC distribution seen *in vivo* (Pries and Secomb, 2005). Experiments also give evidence for a 0.5-1 μm ESL that lines vessel walls (Secomb et al., 2001; Yen et al., 2012). This contributes to vessel resistances that differ significantly from those predicted by glass tubes (Pries et al., 1997). Further studies suggest the ESL has additional roles in shear-stimulated blood flow regulation (Fu and Tarbell, 2013) and in adhesion of platelets (Vink et al., 2000), leukocytes (Mulivor and Lipowsky, 2002), and RBCs to vessel walls (Oberleithner et al., 2015).

Here we use a mathematical model to consider the transport of RBCs as they pass one at a time through an ESL-lined diverging capillary bifurcation. The study helps improve understanding of how ESL properties may affect RBC partitioning, deformation during partitioning, and the extent to which RBCs may interact with the ESL at bifurcations. This, in turn, can give insight into how ESL properties may affect the distribution and activities of other blood transported objects such as oxygen, which is carried by RBCs, other metabolites, drugs, platelets, and white blood cells. This can prove useful in studies of pathologies such as tumor vascularization (Kimura et al., 1996), vascular occlusions (Zhao et al., 2020), sickle cell anemia (Williams and Thein, 2018), and malaria (Fedosov et al., 2011).

Along with liquid plasma, RBCs are the primary constituents of blood by percentage, comprising 40-45% of its volume. At rest, RBCs are shaped like biconcave discs with a diameter of about 8 μm and a width of about 2 μm . They have a concentrated hemoglobin solution interior, a lipid bilayer membrane, and a cytoskeleton anchored into that membrane. This combination produces a viscoelastic response to deformation. RBCs are highly deformable and capable of passing through capillary vessels with diameters as small as approximately 2.7 μm (Secomb and Pries, 2013). Their flexibility and finite size contribute to the nonuniform partitioning seen at diverging vessel bifurcations.

During experiments RBCs have undergone either “classical partitioning” or “reverse partitioning”. In classical partitioning, the high flow downstream branch gets

disproportionately more RBCs than the other branch. For example, the high flow branch may take 75% of the total blood flow and 90% of the RBCs. The phenomenon has been frequently referred to as the Zweifach-Fung effect (Svanes and Zweifach, 1968; Fung, 1973) and/or plasma skimming. To explain the Zweifach-Fung effect, Fung (1973) considered a circle centered on a separating background fluid streamline in a bifurcation (separates blood entering high flow branch from blood entering low flow branch). He explained that the finite size of the circle should lead to shear and pressure forces that point the circle’s trajectory towards the high flow branch (cell screening). For plasma-skimming, shear-induced migration of RBCs away from vessel walls create cell-free layers near the wall that low flow branches sample from during partitioning. This leads to a higher fraction of plasma in those branches (Li et al., 2012). In “reverse partitioning”, the high flow downstream branch gets fewer RBCs, e.g. 75% of the blood flow and only 60% of the red blood cells. Past studies (see Balogh and Bagchi (2018)) for a more thorough review) suggest this may be due to asymmetric upstream activity including situations where RBCs entering the bifurcation typically enter on the low flow, instead of high flow, side of the bifurcation (skewed hematocrit profile). Strong evidence suggests reverse partitioning occurs relatively frequently and that it plays an important role in microvascular RBC distribution (Balogh and Bagchi, 2018; Mantegazza et al., 2020a).

Here, due to the simplified and symmetric nature of the study, only classical partitioning is considered. This is especially because of the added focus in this initial study on more specific details of RBC dynamics including RBC deformation and ESL penetration. Past results indicate that important parameters for partitioning include the fraction of bulk blood entering a branch, the ratio of the two daughter vessel diameters, the size of the mother vessel, the average hematocrit in the region, and the upstream hematocrit distribution (Pries et al., 1989). More recent studies considered the effects of varying downstream hematocrits on partitioning (Chang et al., 2017) and on how successive bifurcations may affect upstream hematocrit distributions and the resulting partitioning (Balogh and Bagchi, 2018; Pskowski et al., 2021; Ye et al., 2019). Some of these studies and results specific to the ESL’s effect on partitioning are discussed below.

Using a model, Barber et al. (2008) showed that RBC partitioning behavior in small capillary bifurcations at low RBC concentrations, or hematocrits, could be explained by three clearly defined effects. In the finite size effect, the finite size of the RBC limits how close the RBC’s center of mass can get to straight vessel

walls. Assuming cells follow background fluid streamlines and are inhibited by this finite size effect can, in fact, explain a large majority, but not all, of typical nonuniform RBC partitioning behavior where high flow branches claim a disproportionately large percentage of red blood cells. In the migration effect, which is due to the flexibility of the RBC, RBC's tend to migrate towards the center of a vessel upstream of a bifurcation. This moves cells that are near low flow branches closer to high flow branches and causes high flow branches to claim even more RBCs than usual and produces more nonuniform partitioning. In the obstruction effect, RBCs that obstruct a downstream branch tend to be pulled into that branch in order to maintain flow conservation downstream of the cell. This effect tends to pull RBCs near high flow branches into low flow branches instead, which encourages more uniform partitioning. A later study by Barber et al. (2011) showed that RBC interactions cause more uniform partitioning, in general. In both cases, Barber's quantitative results for both single (Barber et al., 2008) and paired (Barber et al., 2011) cells agreed well with Pries et al.'s (Pries et al., 1989; Pries and Secomb, 2005) empirically derived RBC partitioning function.

The endothelial glycocalyx (EGL) is made of two semi-distinct layers of membrane-bound macromolecules. The inner layer has been observed to have a quasi-periodic matrix structure (Squire et al., 2001) associated with bush-like configurations of fibers (Rostgaard and Qvortrup, 1997) anchored into the endothelial cells that form the vessel wall. This layer extends approximately 0.05-0.4 μm from the vessel wall (Curry et al., 2020). It then transitions into an outer layer, often referred to as the endothelial surface layer, or ESL. The ESL is made up of a more porous, loosely structured gel-like solution (Curry et al., 2020) which extends from the inner layer out into the vessel lumen a distance of, when combined with the inner layer, approximately 1 μm or more (Secomb et al., 2001; Yen et al., 2012).

The structure and function of these two layers has been studied extensively. Often, researchers have looked at properties of one of the layers while neglecting the other. This has sometimes led to confusion in terminology and the state and role of the osmotic pressure differences across the layers (Weinbaum et al., 2007; Curry et al., 2020). A primary function of the inner layer is its role as a molecular sieve for plasma proteins at the microvascular wall (Levick, 2004). This results in a significant colloidal osmotic pressure drop across the layer of approximately $1.5 \times 10^2 \text{ dyn/cm}^2$, placing structural components in the inner layer in a state of compression (Weinbaum et al., 2007). At the same time, observations suggest that flowing RBCs (≥ 20

$\mu\text{m/s}$) do not invade the EGL while slower or stationary RBCs penetrate the EGL region (Vink and Duling, 2000). This suggests the outer layer, in general, resists compression. Based on the hypothesis that the structural components in the outer layer, filaments, resist flattening because of the colloidal osmotic pressures generated by plasma proteins in the ESL, Secomb et al. (1998, 2001) found that an osmotic pressure increase of 20 dyn/cm^2 is sufficient to exclude flowing RBCs from the layer, yet small enough to allow an RBC to completely compress the layer while stationary (Vink and Duling, 1996). This predicted increase in osmotic pressure places the ESL structural components in a state of tension rather than compression. These varying predictions (tension versus compression) for osmotic pressure differences in the EGL can be readily explained by the bi-layer model.

RBCs interact most with the outer ESL as they pass through the microvasculature and we limit our considerations to that layer. Besides its resistance to compression, the ESL is also known to impede the flow of plasma, which significantly increases flow resistance in microvessels when compared to *in vitro* studies of vessels with equal dimensions (Secomb et al., 2002). Modeling the ESL as a porous medium with a corresponding hydraulic resistivity and a resistive osmotic pressure difference, Secomb et al. (1998) was able to obtain vessel flow resistance estimates that agreed with experiment.

The above modeling results suggested that the ESL's ability to resist flow (hydraulic resistivity) and compression (osmotic pressure difference) play a strong role in these two important experimentally observed phenomenon, the significant difference between flow resistance *in vivo* vs *in vitro* and the ability for RBCs to take on different shapes and penetrate the ESL depending on flow speed. Because of these observations, we chose to include these two properties in our model of the ESL. In addition, accurate modeling of RBC-ESL interactions should include model components that can affect RBC penetration of the ESL by pushing cells away from the vessel wall, in this case the osmotic pressure difference (Secomb et al., 1998).

Besides hydraulic resistivity and osmotic pressure difference, there are other potentially important ESL properties including ESL width (Secomb et al., 1998, 2001), structure (Curry et al., 2020), and adhesivity (Vink and Duling, 2000). As observed *in vivo*, the ESL is not a uniform thickness in all vessels, and is often irregular in structure (Curry et al., 2020). This can have an effect on flow dynamics. For instance, the results in Secomb et al. (1998) show that varying the ESL width (still assuming uniform structure) could change the flow resistance. To simplify geometries considered and main-

tain study feasibility in terms of number of free parameters, the model used here neglects ESL irregularity and instead assumes a homogeneous ESL of uniform width. Additionally, sufficient cell penetration into the ESL may lead to cell adhesion (Vink and Duling, 2000), which can, for instance, slow cells as they move down a vessel. Again, to maintain model and study simplicity, we have not this factor. Despite these omissions, including just the resistance to flow and compression allowed us to reproduce results that agree relatively well with experiment including similar flow resistance estimates (see Secomb et al. (1998) for a similar validation) and partitioning estimates (Pries and Secomb, 2005).

In addition to the previously mentioned studies, models have been used in many other contexts to better understand partitioning behavior at bifurcations. Barber et al. (2011) used a similar model to not only show cell-cell interactions generate more uniform partitioning, they also identified three main types of interactions: trade-off interactions, herding interactions, and following interactions. Trade-off interactions, the more prevalent of the three main types, produced more uniform partitioning overall, while herding and following interactions promoted less uniform partitioning. Trade-off interactions happen when the leading cell entering a daughter branch causes the following cell to enter the alternative branch. When the front cell enters one branch, it effectively carries a large amount of volume with it into that branch. To maintain the flow split in the bifurcation (e.g. 25% out one daughter branch and 75% out the other), the back cell enters the opposite branch. Herding interactions happen when the following cell entering a daughter branch causes the leading cell to enter the same branch. Similarly, following interactions occur when the leading cell entering a daughter branch causes the following cell to enter the same branch. In the two latter cases, this is caused by the cells being very close together which, in turn, causes the cells to move as a single object.

Balogh and Bagchi (2018) used a model to study many RBCs in a large three-dimensional network of vessels featuring multiple successive bifurcations, both converging and diverging. They identified and studied some underlying cellular scale mechanisms including reverse partitioning. They found two main cell mechanisms that are responsible for increased reverse partitioning: asymmetry in the RBC distribution upstream of diverging vessel bifurcations and temporary and fluctuating increases in the RBC concentration in the bifurcation region. Asymmetry in RBC distributions arises due to the partitioning behavior at previously encountered bifurcations and is more likely to affect partitioning in series of bifurcations in relatively close succes-

sion. In cases of increased concentration of cells near bifurcations, reverse partitioning arises due to a mechanism analogous to the previously described trade-off interactions.

Models have also been used to understand the effects of the ESL outside of microvessel bifurcations. Damiano (1998) used mixture theory to model the ESL as a linearly elastic solid under deformation. He found that the presence of the ESL contributed to a significant increase in resistance and reduction in hematocrit in capillary tubes. These results matched qualitatively with experimental results. Hariprasad and Secomb (2012) later modeled the effect of the ESL on RBC shapes. They found that the ESL led to two different possible steady state shapes that might result as they travel along the tube. These differences were observed for differing values of the hydraulic resistivity in the ESL chosen from a range of physiologically realistic values. Despite these efforts, and others (Obrist et al., 2010; Lückner et al., 2015), such studies do not consider both the ESL and RBC partitioning in conjunction.

Relatively little work has been done to consider how the ESL may affect partitioning. Chang et al. (2017) studied how occlusive feedback could encourage more uniform partitioning. In occlusive feedback, downstream vessels with higher hematocrits raise vessel resistance, lower vessel flow, and claim fewer cells in the future reducing the hematocrit back to lower levels. Their consideration of the ESL, however, was limited to how higher hematocrits and how the ESL affects the flow resistance in downstream branches with more/thicker ESL encouraging more uniform partitioning. Other non-ESL focused studies have also been used to make ESL-related conjectures. For instance, Barber et al. (2011) predicted that the ESL would reduce the effective vessel width of the vessel, which, based on their results, would lead to more downstream vessel obstruction and more nonuniform partitioning. Additionally, they predicted that the layer would reduce the tendency of cells to linger at the bifurcation thereby reducing cell-cell interactions, which would also lead to more nonuniform partitioning. Other experimentalists have put forth similarly motivated conjectures like these (Pries et al., 1997; Desjardins and Duling, 1990). Microfluidic studies have also conjectured that the presence of the ESL may not significantly affect partitioning, based on their results agreeing relatively well with *in vivo* results (Mantegazza et al., 2020a,b). These studies, however, focused primarily on network effects and without any ESL they are unable to comment on how the ESL affects red blood cell dynamics. Studies specifically targeting the ESL's role in partitioning that include the corresponding red blood cell dynamics are not available, to our knowledge.

Here we consider both the ESL and RBC partitioning using a two-dimensional mechanical model of isolated RBCs passing one at a time through a diverging capillary bifurcation. The focus here is restricted to three major aspects of RBC dynamics in a single diverging capillary bifurcation. The first major aspect is the partitioning of RBCs into one or the other downstream daughter branch. The second major aspect is the deformation of cells as they pass through the bifurcation. The third is how deeply the RBCs penetrate the ESL (ESL penetration) when they encounter the ESL. While other events can occur (e.g. oxygen release), to maintain a feasible study, we consider just these three major aspects whose consideration requires only a strictly mechanical model.

As previously discussed, RBC partitioning can affect the distribution of RBCs, and other blood constituents, throughout the microvasculature.

Mechanical deformation of RBCs has been linked to release of various metabolites including adenosine triphosphate (ATP) and nitric oxide (NO). For instance, Bor-Kucukatay et al. (2003) devised an experimental study *in vitro* that showed a significant link between NO concentration and RBC deformability as quantified by an elongation index. Following experimental studies by Forsyth et al. (2011, 2012), Zhang et al. (2018) developed a model that predicts ATP release using the level of shear stress experienced in the cell membrane as well as its curvature. They predicted that the highest rates of these factors are observed in diverging bifurcations, indicating that the highest rates of ATP release are located at vessel bifurcations as well.

Deeper ESL penetration has been associated with impaired microvascular function and with increased damage in the ESL that can occur in multiple pathological scenarios including cardiovascular disease, end-stage renal disease, stroke, and thrombosis (Lee et al., 2014; Weisel and Litvinov, 2019). RBC penetration of the ESL has also been associated with a greater likelihood for cellular adhesion. For instance, Vink et al. (2000) used oxidized low-density lipoproteins to damage the ESL and reduce the gap between RBCs and endothelial cells (ECs). The gap size, or penetration depth, correlated well with the number of platelets observed to adhere to the EC surface. Further evidence is offered by Oberleithner et al. (2015) where ESL damage, correlated with ESL penetration, led to an increase in adhesive interactions between RBCs and ECs via endothelial structures such as epithelial sodium channels. While there tends to be more interest in adhesion of platelets and leukocytes due to their important thrombotic and inflammatory roles, RBC adhesion has not only been seen to occur, it has also been correlated with

microcirculatory disorders (Yedgar et al., 2008). RBCs that have adhered to walls can significantly disrupt normal blood flow in vessels and alter the hemodynamics taking place in a given system. In addition, RBC adhesion can further result in increased RBC damage and impaired RBC function (Oberleithner, 2013).

Secomb et al. (2007) developed a two-dimensional viscoelastic model similar to the one used in these studies. It was calibrated using data on RBC motion in shear flow (tank-treading). It was then used to reproduce the physiological shape of an RBC as it passed along a bifurcation made up of smooth vessels. In later work, Barber et al. used the model to reproduce partitioning estimates for both single (Barber et al., 2008) and paired (Barber et al., 2011) cells. Their predictions of partitioning behavior at low hematocrit and for the rate at which partitioning changes as hematocrit is increased agreed well with Pries et al.'s (Pries et al., 1989; Pries and Secomb, 2005) empirically derived RBC partitioning function. Similarly, the ESL model used here was used by Secomb et al. (1998) to produce estimates for vessel resistances that agreed with experiment. This gives evidence that the models used here are capable of producing physiologically realistic and relevant insights.

By combining these two past models, one for RBC motion and the other for ESL dynamics, we investigate the effects of varying the hydraulic resistivity and the osmotic pressure difference between the ESL and the free flowing region (referred to as the “osmotic pressure difference in the ESL”, or simply as the “osmotic pressure difference” henceforth). The results show that decreasing the hydraulic resistivity and osmotic pressure difference promotes more nonuniform partitioning, more ESL penetration, and, usually, leads to less deformation. In addition, we show that physiologically realistic parameters of hydraulic resistivity and osmotic pressure within the ESL can lead to sufficient penetration by RBCs at diverging vessel bifurcations for possible cell adhesion to take place in pathological scenarios.

2 Methods

In the following subsections details for the computational model and its analysis are given. As a summary, the RBC is modeled as a two-dimensional network of viscoelastic elements surrounded by fluid, as done previously in Barber et al. (2011). The ESL is modeled as a porous medium that resists compression, which combines approaches from Hariprasad and Secomb (2012) and Secomb et al. (1998). The blood vessel bifurcation configuration used (Figure 1a) and its geometry and accompanying boundary conditions were chosen to approximately match the vessel geometries used in Barber

et al. (2008) and Hariprasad and Secomb (2012). A finite element program, FlexPDE (PDE Solutions Inc, 2021), is used to solve the coupled fluid-solid equations for the membrane velocities at prescribed times. An adaptive time integrator uses those velocities to obtain RBC trajectories. Multiple metrics are used to quantify how varying ESL porosity and rigidity affects RBC partitioning (Barber et al., 2008), deformation (Barber and Zhu, 2019), and penetration of the ESL.

2.1 Mathematical Modeling

The fluid in the microvessel bifurcation is modeled using viscous flow equations for the free flowing plasma and porous media flow equations for the fluid in the ESL. The RBC itself is modeled using interconnected viscoelastic and purely viscous elements. Membrane or mechanical equilibrium equations (Evans and Skalak, 1979) are used to couple the fluid and solid models.

2.1.1 Modeling Fluid Flow

The suspending medium in the non-ESL region is assumed to be a low Reynolds number ($O(0.01)$) incompressible flow so that it is well approximated by the Stokes flow equations:

$$\nabla \cdot \boldsymbol{\sigma} = 0; \quad \nabla \cdot \mathbf{u} = 0. \quad (1)$$

$\mathbf{u} = (u(x, y), v(x, y))$ is the two-dimensional velocity field and the corresponding components of stress are:

$$\boldsymbol{\sigma} = \mu(\nabla \mathbf{u} + \nabla \mathbf{u}^T) - p\mathbf{I}. \quad (2)$$

$p(x, y)$ is the pressure field, \mathbf{I} is the identity matrix, and μ is the fluid's dynamic viscosity.

Following past work (Secomb et al., 1998; Hariprasad and Secomb, 2012), the flow in the ESL is modeled by assuming the layer acts as a porous medium that has a relatively high hydraulic resistivity and a width that is roughly $1 \mu\text{m}$ ($w = 1 \mu\text{m}$). In particular, a Brinkman approximation (Brinkman, 1947) models the flow in the ESL by introducing drag on the fluid in the porous medium that is proportional to the fluid's velocity:

$$\nabla \cdot \boldsymbol{\sigma} = \kappa_v(d)\mathbf{u}. \quad (3)$$

The hydraulic resistivity $\kappa_v(d)$ is assumed to depend on the distance to the vessel wall, d , and is given by:

$$\kappa_v(d) = \kappa \frac{1}{2} \operatorname{erfc} \left(\frac{d-w}{L} \right). \quad (4)$$

$\operatorname{erfc}()$ denotes the complementary error function and κ gives the maximum hydraulic resistivity in the layer. The value of $L = 0.157 \mu\text{m}$ was chosen by Secomb et al.

(1998) so that most of the variation in $\kappa_v(d)$ occurs over a distance of around $0.4 \mu\text{m}$, which was shown to produce realistic vessel flow resistance estimates. Accordingly, within $w-0.4/2 = 0.8 \mu\text{m}$ of the vessel wall, $\kappa_v(d)$ is a large approximately constant ($0.96\kappa \leq \kappa_v \leq \kappa$) value and porous flow occurs. Similarly, $\kappa_v(d)$ is approximately zero ($\leq 0.04\kappa$) farther than $w+0.4/2 = 1.2 \mu\text{m}$ away from the wall and Stokes flow occurs. The hydraulic resistivity (and ESL osmotic pressure difference, discussed later) is modeled using a diffuse rather than a sharp boundary because: 1. smoother dynamics result in/near the ESL region, which allows for larger time steps and faster simulations while still maintaining the same level of numerical accuracy and 2. results using a sharp boundary produce similar (though less smooth) dynamics and partitioning behavior suggesting that the choice is relatively unimportant for the final results.

The fluid domain is pictured in Figure 1a with flow coming in on the left through the larger mother vessel and flow exiting out two daughter vessels on the right. The origin is located at the intersection of the three vessel centerlines and the labeled arrows show the positive x and y directions. The length of each vessel, measured from the origin along the vessel centerline to the vessel inlet/outlet, is given by $Lv_0 = Lv_1 = Lv_2 = 5(w_0 - 2w)/2$, consistent with (Barber et al., 2008). The inlet pressure is set to zero and the velocity and pressure's normal derivative (more in Numerical Methods) on the outlets are prescribed to match the flow profile for well-developed flow in a tube with a $1 \mu\text{m}$ thick porous layer with hydraulic resistivity κ along its walls. While this differs from using the flow profile for well-developed flow in a tube with variable hydraulic resistivity of κ_v across its width, the two flow profiles are very similar far away from the outlets. In particular, for the simulations here, the cells are always $> 5 \mu\text{m}$ away from the boundaries where the difference in flow profiles due to the two different outflow conditions are always approximately 0.025%. The first of the two flow profiles, however, was significantly easier to reliably implement in FlexPDE. The boundary conditions at the solid vessel walls are no-slip. Other choices for geometry dimensions (e.g. w and w_0), orientation (e.g. θ_1 and θ_2), and total vessel flux (Q_0) are discussed in Parameter Values and Initial Conditions.

2.1.2 Modeling Red Blood Cells

The two-dimensional red blood cell model represents a cross-section through the center of the cell. It is discretized into a loop of n external nodes that are connected by n external line segments and connected to internal line segments that connect to a single inter-

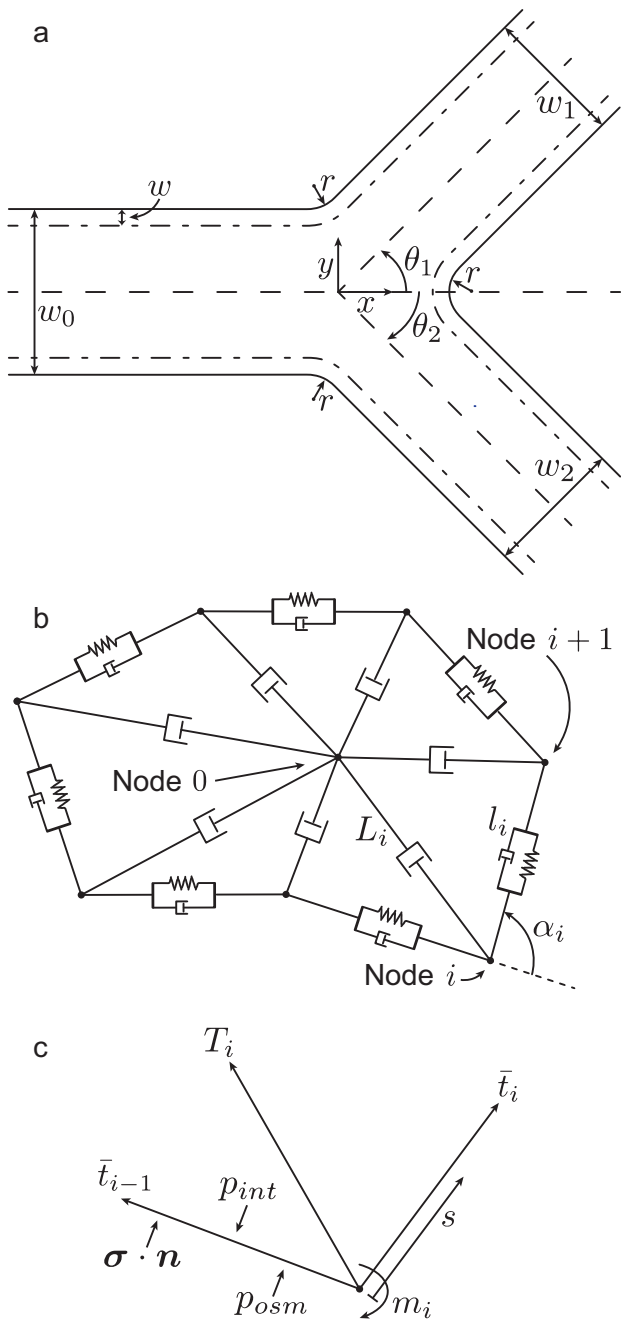


Fig. 1 **a** Geometry of the fluid domain with vessel widths of $w_0 = 10 \mu\text{m}$ and $w_1 = w_2 = 8.35 \mu\text{m}$ including an ESL width of $w = 1 \mu\text{m}$. Daughter branches bifurcate at $\theta_1 = \theta_2 = 45^\circ$ angles from the mother vessel. The radii of the circular arcs that link the vessel walls in the bifurcation are all $r = 2 \mu\text{m}$. The x -axis runs parallel to the axis of the mother vessel, while the y -axis runs perpendicular. **b** The two-dimensional model of a discretized RBC as a set of nodes (e.g. Node i and $i+1$) connected to each other by external viscoelastic elements of length l_i and connected to a central node (Node 0) by internal viscous elements of length L_i . **c** Summary of forces acting on Node i including membrane tensions (\bar{t}_{i-1} and \bar{t}_i), bending resistance (m_i ; curved arrow), internal viscous resistances (T_i), internal pressure (p_{int}), external fluid ($\sigma \cdot \mathbf{n}$) and ESL (p_{osm}) forces. Also included is the arclength s that gives the distance from Node i along the i^{th} external element and is used when calculating force balances for each node

nal node (Figure 1b). Using $n = 20$ produces results that agree with experiment (Secomb et al., 2007; Barber et al., 2008, 2011; Hariprasad and Secomb, 2012). To represent the membrane's viscoelastic resistance to deformation, each external segment is modeled as a viscous and an elastic component connected in parallel. To represent the membrane's resistance to bending, a bending moment is introduced at each external node between each external segment. Finally, to represent both the effects of the internal viscosity of the cell as well as the viscous resistance of the cell membrane to out-of-plane deformations, each internal segment is comprised of a solely viscous component.

The i^{th} external node at position \mathbf{x}_i is connected to the i^{th} internal segment and external segments labeled $i-1$ (between Node $i-1$ and i) and i (between Node i and $i+1$). The internal node is labeled as Node 0. During deformation, the i^{th} external segment experiences a tension force $t_i(s)$, a shear force $q_i(s)$, and a bending moment $m_i(s)$, where s is the distance along the element from node i toward node $i+1$, l_i is the length of the i^{th} external segment, and $0 \leq s \leq l_i$.

In addition to external fluid forces, the model also accounts for ESL-mediated forces that can arise when the red blood cell compresses the ESL. Secomb et al. (1998) modeled the ESL's resistance to compression by assuming the ESL exhibits a slightly elevated colloid osmotic pressure due to the adsorption of plasma protein molecules. Following Secomb et al. (1998), the effective pressure resulting from this osmotic pressure difference is modeled in the same way as the hydraulic resistivity:

$$p_{osm} = \Delta\pi_p \frac{1}{2} \operatorname{erfc} \left(\frac{d-w}{L} \right) \quad (5)$$

$\Delta\pi_p$ is a constant corresponding to the maximum difference between the osmotic pressures in the ESL and the vessel lumen. p_{osm} has a minimal direct effect on the fluid motion and so is not found in the fluid equations. It directly affects the red blood cells that penetrate the ESL with the osmotic or resistive forces in the compacted ESL pushing the RBCs back away from the vessel wall. The resulting altered RBC motion, in turn, alters the nearby fluid motion through the no-slip boundary conditions on the RBC boundary.

An internal pressure is also used in the model. While many other two-dimensional approaches model the interior fluid of the RBC using incompressible fluid equations, this model has been explicitly calibrated and validated in Secomb et al. (2007) and Barber et al. (2008) using experimental pictures of RBC cross-sections. Such cross-sections are not incompressible in the sense that their visible two-dimensional cross-sectional areas can and do fluctuate during experiments. Despite this, three-

dimensional red blood cell volume conservation (due to fluid incompressibility) and membrane area conservation (the RBC membrane has approximately constant surface area over the time scales considered here) do cause such cross-sectional areas to conform to approximate (not strict) area conservation. This is enforced in the model by introducing a pressure to the interior of the cell:

$$p_{int} = k_p \left(1 - \frac{A}{A_{ref}} \right). \quad (6)$$

A_{ref} is a constant reference area and k_p is a constant giving the strength with which the approximate area conservation is enforced.

The average tension in the i^{th} external segment is given by:

$$\bar{t}_i = k_t \left(\frac{l_i}{l_0} - 1 \right) + \mu_{ext} \frac{1}{l_i} \frac{dl_i}{dt}. \quad (7)$$

k_t is the elastic modulus, l_0 is the reference length of the segment, and μ_{ext} is the viscosity. The first and second term on the right hand side correspond to the elastic and viscous components of the element. Linear elastic elements and viscous elements that are linear with respect to dl_i/dt are used for simplicity. The internal segments are purely viscous with the average tension in the i^{th} internal segment given by:

$$T_i = \mu_{int} \frac{1}{L_i} \frac{dL_i}{dt}. \quad (8)$$

μ_{int} is the viscosity and L_i is the length of the i^{th} internal segment.

The resistance of the cell membrane to bending can be modeled by including bending moments at each external node:

$$m_i(s=0) = -\frac{k_b \alpha_i}{l_0} \quad (9)$$

where k_b is the bending modulus and α_i is the exterior angle between external segments $i-1$ and i .

2.1.3 Model Coupling

The coupling of the cell membrane stresses with the external stresses are given by the following equations of membrane or mechanical equilibria (Evans and Skalak, 1979):

$$\frac{dt_i}{ds} = -g_i; \quad \frac{dq_i}{ds} = -f_i; \quad \frac{dm_i}{ds} = q_i. \quad (10)$$

$g_i(s)$ and $f_i(s)$ are the tangential and normal components of the fluid stresses.

The external fluid stresses, osmotic pressure difference, and interior pressure combine to give the following equation for the external stresses acting upon the i^{th} external segment:

$$g_i = \mathbf{t}_i^T \boldsymbol{\sigma} \mathbf{n}_i; \quad f_i = \mathbf{n}_i^T \boldsymbol{\sigma} \mathbf{n}_i + p_{int} - p_{osm}. \quad (11)$$

\mathbf{n}_i and \mathbf{t}_i are the unit vectors normal and tangential to the i^{th} external segment and point away from and counterclockwise to the cell interior, respectively. When g_i is a positive value, the fluid pulls on the cell membrane in a counterclockwise direction while a positive value of f_i corresponds to the fluid pulling the membrane outward.

Integrating the above expression for dm_i/ds gives the average shear stress, \bar{q}_i , in the external segments in terms of the exterior angles at either end of the i^{th} segment, angles α_i and α_{i+1} :

$$\bar{q}_i = \frac{k_b(\alpha_i - \alpha_{i+1})}{l_i l_0} \quad (12)$$

Appropriate integration and manipulation of the remaining mechanical equilibrium equations yields the forces acting on the endpoints of the external segments:

$$\begin{aligned} t_i(0) &= \bar{t}_i + \frac{1}{l_i} \int_0^{l_i} (l_i - s) g_i(s) ds; \\ t_i(l_i) &= \bar{t}_i + \frac{1}{l_i} \int_0^{l_i} s g_i(s) ds; \\ q_i(0) &= \bar{q}_i + \frac{1}{l_i} \int_0^{l_i} (l_i - s) f_i(s) ds; \\ q_i(l_i) &= \bar{q}_i + \frac{1}{l_i} \int_0^{l_i} s f_i(s) ds. \end{aligned} \quad (13)$$

The internal segments are not acted upon by any fluid.

At the i^{th} external node, the equilibrium of forces can be written as the following equation:

$$\begin{aligned} t_i(0) \mathbf{t}_i - t_{i-1}(l_{i-1}) \mathbf{t}_{i-1} - q_i(0) \mathbf{n}_i \\ + q_{i-1}(l_{i-1}) \mathbf{n}_{i-1} + T_i \mathbf{T}_i + \mathbf{f}_{i,lub} = 0. \end{aligned} \quad (14)$$

\mathbf{T}_i is the unit vector pointing into the cell interior along the i^{th} internal segment and $\mathbf{f}_{i,lub}$ are additional ‘‘lubrication’’ forces that are set to zero *unless* a cell node is within 0.01 μm from another object. $\mathbf{f}_{i,lub}$ is discussed in more detail in Numerical Methods. At the internal node, the equilibrium of forces can be written as:

$$\sum_{i=1}^n T_i \mathbf{T}_i = 0. \quad (15)$$

These ‘‘nodal equations’’ form a system of $2(n+1) = 42$ linear equations for each red blood cell. They describe the balance of forces at each node in terms of the unknown nodal velocities, $\{\mathbf{u}_i = \dot{\mathbf{x}}_i\}_{i=0}^n$, and unknown fluid velocities near the external elements.

These equations are further coupled to the surrounding fluid through the use of no-slip conditions at the cell membrane. The velocity of the membrane along the i^{th} external element, $\mathbf{u}_{i,m}(s)$, is estimated using linear interpolation and the unknown membrane nodal velocities:

$$\mathbf{u}_{i,m}(s) = \frac{l_i - s}{l_i} \mathbf{u}_i + \frac{s}{l_i} \mathbf{u}_{i+1} \quad (16)$$

The fluid velocities along the membrane are required to match these interpolated membrane velocities yielding boundary conditions for the fluid on the cell boundary that involve the $2(n+1)$ unknown membrane nodal velocities.

The resulting coupled fluid-nodal equations for the force balance in this system involve both unknown membrane nodal velocities and unknown fluid velocities. FlexPDE solves (effectively a solely spatial solve) these coupled equations to obtain estimates for all unknown instantaneous velocities at that particular time. The membrane nodal velocities that are found in this way can then be used to obtain the long-term motion of the red blood cells.

2.2 Numerical Methods

The coupled system of equations describing the motion of the red blood cells and the surrounding plasma is solved using the finite-element package FlexPDE. Cubic finite elements are used. The solvers utilized by FlexPDE are structured in such a way that the incompressibility condition $\nabla \cdot \mathbf{u} = 0$ cannot be specified exactly. Instead, we use the condition that:

$$\nabla^2 p = K \nabla \cdot \mathbf{u}. \quad (17)$$

Choosing $K = \mu/L_{res}^2 = 1 \times 10^8$ dyn·s/cm⁴, where $L_{res} = 1 \times 10^{-5}$ cm = 0.1 μm is the approximate desired length scale of incompressibility resolution, was found to sufficiently approximate the incompressibility of the fluid (Secomb et al., 2007; Barber et al., 2008). Using this Laplacian-based penalty method for approximate incompressibility requires prescribing additional boundary conditions for the pressure. We set $\partial p / \partial \mathbf{n} = 0$ at all but the inlets and outlets (see 2.1.1). For the large value of K chosen, results do not seem dependent on these extra boundary conditions.

During simulations, red blood cells can experience relatively rapid changes in dynamics as they encounter vessel walls or rapid changes in ESL properties. The adaptive mesh generator utilized by FlexPDE helps better resolve such changes by creating an increasingly refined mesh in narrow channels between red blood cells

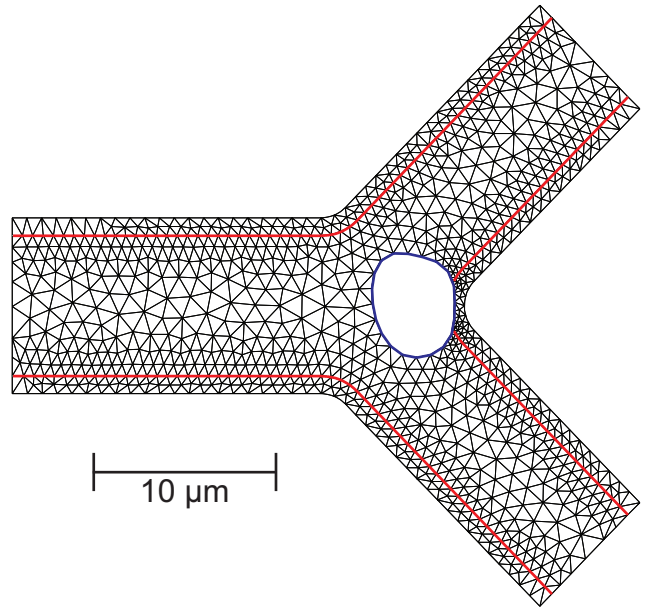


Fig. 2 A representative example of the discretized flow domain. Triangle edges and corresponding nodes fall along the ESL boundary feature (red). The feature at the far wall is broken into two sections no less than 0.1 μm from the cell. This is to prevent very small triangles in the gaps between the red blood cell and ESL boundaries and resulting slow converging iterative methods due to poorly conditioned matrices

and other objects, as well as in regions of sharp changes in the ESL hydraulic resistivity and osmotic pressure difference. In particular, FlexPDE refines the mesh so that its estimates for local relative errors are less than $1e-3$. For a representative example of the discretized flow domain, see Figure 2.

In extreme cases where red blood cells are within 0.01 μm of the vessel wall ($\ll L_{res} = 0.1 \mu\text{m}$), the penalty condition is unable to appropriately enforce incompressibility in the fluid. This results in cells that unrealistically collide in finite time with the vessel wall. In fact, when red blood and endothelial cells are close enough to each other, the surface roughness on the cells (e.g., red blood cells have their own glycocalyx that protrudes from the cell approximately 0.01 μm (Heinrich et al., 2001)) begins to initiate solid-solid interactions with each other and limit how close those cells can become. To limit such collisions we follow Barber (2009) and augment the nodal equations for nodes within 0.01 μm of a vessel wall or other object by adding a non-zero lubrication force, $\mathbf{f}_{i,lub}$, that resists collisions.

To derive a reasonable estimate for such a resistive force, the cell node in question is temporarily replaced by a short (0.1 μm) lubrication segment parallel to the other object. This better represents the physiological membrane as membranes typically do not have corners and the short lubrication segment approximates what

the region would look like if the corner represented by the node was smoothed. Lubrication theory is then used to derive an estimate for the force acting on the corner in terms of the relative velocities between the two objects:

$$\mathbf{f}_{i,lub} = -\mu \left(\left(\frac{0.1}{d_l} \right)^3 \mathbf{n}_w \mathbf{n}_w^T + \left(\frac{0.1}{d_l} \right) \mathbf{t}_w \mathbf{t}_w^T \right) \mathbf{u}_r \quad (18)$$

d_l is the distance between the two objects, \mathbf{n}_w points from the node to the closest point on the other object, \mathbf{t}_w is a vector perpendicular to \mathbf{n}_w , and \mathbf{u}_r is the relative velocity between the two objects. We also performed studies with increased penalty value K and verified that adding lubrication elements produced similar results that more strictly enforcing incompressibility produced except that increasing K significantly increased computation time (approximately $\propto K$).

For any given time step, t_j , and set of nodal positions, $\{\mathbf{x}_i\}_{i=0}^n$, solving the coupled fluid-nodal equations using FlexPDE yields an estimate for the instantaneous velocity for each node on the membrane. We can think of this as a complicated function that returns the nodal velocities: $\mathbf{u}_i = \mathbf{g}_i(t_j, \mathbf{x}_0, \dots, \mathbf{x}_n)$. The positions, \mathbf{x}_i , can be found by integrating the ordinary differential equations $d\mathbf{x}_i/dt = \mathbf{g}_i(t, \mathbf{x}_0, \dots, \mathbf{x}_n) = \mathbf{u}_i$ for all i . Despite adaptive spatial refinement and use of lubrication elements, however, using a reasonable constant time step (e.g. approximately 1 ms) and a standard time integrator like forward Euler or the explicit trapezoidal method can still result in unrealistic membrane/boundary overlap. The integration with respect to time is therefore performed using an adaptive second order Runge-Kutta scheme:

$$\begin{aligned} \mathbf{u}_{i,c}^j &= \mathbf{g}_i(t_j, \mathbf{x}_{0,c}^j, \dots, \mathbf{x}_{n,c}^j) \\ \mathbf{x}_{i,p}^{j+1} &= \mathbf{x}_{i,c}^j + dt_p \mathbf{u}_{i,c}^j \\ \mathbf{u}_{i,p}^{j+1} &= \mathbf{g}_i(t_{j+1}, \mathbf{x}_{0,p}^{j+1}, \dots, \mathbf{x}_{n,p}^{j+1}) \\ \mathbf{x}_{i,c}^{j+1} &= \mathbf{x}_{i,c}^j + dt_c \left(\frac{2dt_p - dt_c}{2dt_p} \mathbf{u}_{i,c}^j + \frac{dt_c}{dt_p} \mathbf{u}_{i,p}^{j+1} \right). \end{aligned} \quad (19)$$

Subscript p corresponds to the ‘‘predictor’’ step while subscript c corresponds to the ‘‘corrector’’ step. The superscript j indicates the time step, t_j , currently being explored. When $dt_p = dt_c$, this becomes the explicit trapezoidal or Heun’s method. If $dt_p \neq dt_c$, the method is still second order accurate and has the same stability region as Heun’s method, as determined by dt_c . Here dt_p and dt_c are both picked so that the distance between any two points on the boundaries (cell membrane and vessel wall) changes by no more than 10%, or 1% in the ESL regions (when the cell’s distance to the vessel wall is $< 1 \mu\text{m}$). A maximum time step of 1 ms was also enforced.

2.3 Parameter Values and Initial Conditions

Red blood cell parameter values were taken from Barber et al. (2008). Those values were originally derived in Secomb et al. (2007) by adjusting experimentally obtained parameter values for red blood cells to produce observed rotational motion (tank-treading behavior) of red blood cells subjected to shear flow. The resulting parameters are a membrane shear elasticity of $k_t = 0.012 \text{ dyn/cm}$, a membrane bending modulus of $k_b = 9 \times 10^{-12} \text{ dyn-cm}$, a membrane viscous resistance to in-plane deformation of $\mu_m = 2 \times 10^{-4} \text{ dyn-s/cm}$, a membrane viscous resistance to out-of-plane deformation of $\mu'_m = 1 \times 10^{-4} \text{ dyn-s/cm}$, a reference length for the external segments of the membrane of $l_0 = 0.97 \mu\text{m}$, and a reference length for the cross-sectional area of a red blood cell of $A_{ref} = 22.2 \mu\text{m}^2$. For the surrounding fluid, the viscosity is set at $\mu = 1 \text{ cP}$. All parameters are given in Table 1.

The branching domain considered here is as seen in Figure 1 and is representative of a diverging vessel bifurcation in a capillary network. The mother branch is taken to have a width of $8 \mu\text{m}$, not including the width of the ESL. To maximize consistency with Barber et al. (2008), the widths of the vessels not including the ESL were chosen so that $(w_0 - 2w)^3 = (w_1 - 2w)^3 + (w_2 - 2w)^3$, which arteriolar vessel diameters have been shown to approximately obey (Mayrovitz and Roy, 1983), and the condition that the two daughter branches are the same size yields $6.35 \mu\text{m}$ for the daughter vessel widths. We also consider equal branching angles of 45° . Past studies have suggested that the branching angle does not significantly affect cell partitioning (Pries and Secomb, 2005; Barber et al., 2008). The total flow rate Q_0 was set to be $8 \mu\text{m}^2/\text{ms}$ for cases including an ESL, and $Q_0 = 10 \mu\text{m}^2/\text{ms}$ when κ_v was set to zero corresponding to a vessel completely stripped of any ESL and effectively $10 \mu\text{m}$ wide. This yields an average velocity in the non-ESL portions of the mother vessels of approximately $1 \mu\text{m}/\text{ms}$. The fraction of bulk blood flow into the upper daughter branch or the branch’s ‘‘flow split’’ is given by $\Psi_1 = Q_1/Q_0$.

Our simulations suggest that the choice for the magnitude of Q_0 ($\pm 50\%$) does not significantly affect red blood cell dynamics. This is consistent with the observation that when \mathbf{u} and p solve Stokes equations, so do $c\mathbf{u}$ and cp , where c is any constant and the boundary conditions are appropriately rescaled. In such cases expected dynamics (partitioning behavior, deformation, penetration) are exactly the same with the exception that they occur either more slowly or more quickly. In our case, appropriate rescaling of boundary conditions is not possible due to the elastic components in the cell.

Table 1 Parameters in the model and the values used

Parameter	Description	Value	Units
k_p	Approximate area conservation enforcement strength	50	dyn/cm ²
k_t	Membrane shear elasticity	1.2×10^{-2}	dyn/cm
k_b	Membrane bending modulus	9×10^{-12}	dyn-cm
μ_{ext}	External element viscosity	2×10^{-4}	dyn-s/cm
μ_{int}	Internal element viscosity	1×10^{-4}	dyn-s/cm
μ	Dynamic viscosity of the surrounding fluid	1×10^{-2}	dyn-s/cm ²
l_0	Reference length of the external membrane segments	0.97	μm
A_{ref}	Reference area for the cross-sectional area of an RBC	22.2	μm^2
K	Penalty constant for enforcing incompressibility	1×10^8	dyn-s/cm ⁴
δ_{lub}	Threshold below which lubrication forces are calculated	1×10^{-2}	μm
κ	Maximum hydraulic resistivity for the ESL	$0 - \infty$	dyn-s/cm ⁴
$\Delta\pi_p$	Maximum osmotic pressure difference	$0 - \infty$	dyn/cm ²

Table 2 The combinations of maximum hydraulic resistivities (κ in dyn-s/cm⁴) and osmotic pressure differences ($\Delta\pi_p$ in dyn/cm²) explored in the Results section

κ	$\Delta\pi_p$	Description
0	0	Absent ESL/denuded vessel wall
1×10^6	20	Low pathological κ , low $\Delta\pi_p$
1×10^7	20	Low physiological κ , low $\Delta\pi_p$
1×10^8	20	High physiological κ , low $\Delta\pi_p$
1×10^6	200	Low pathological κ , high $\Delta\pi_p$
1×10^7	200	Low physiological κ , high $\Delta\pi_p$
1×10^8	200	High physiological κ , high $\Delta\pi_p$
∞	∞	Impermeable ESL (effectively an 8 μm wide mother vessel)

Nonetheless, simulations suggest that solutions/results are approximately rescalable and flux-independent.

To better understand the effects of the ESL's hydraulic resistivity and osmotic pressure differences on partitioning, deformation, and red blood cell penetration of the ESL, simulations were performed using multiple sets of hydraulic resistivity and osmotic pressure difference values. These sets are listed in Table 2. Setting $\kappa = \Delta\pi_p = 0$ corresponds to a capillaries where the ESL has been eliminated. $\kappa = \Delta\pi_p = \infty$ corresponds to a capillary whose ESL is completely impenetrable by flow and by red blood cells. This is equivalent to considering red blood cell motion in a diverging microvessel bifurcation that has an 8 μm mother vessel and no ESL. For the other cases, $\kappa = 1 \times 10^6$ dyn-s/cm⁴ represents a hydraulic resistivity that is low in comparison to normal physiology but has been observed experimentally in certain pathological conditions (Pries et al., 1998). $\kappa = 1 \times 10^7$ dyn-s/cm⁴ is on the lower end of the normal physiological range while $\kappa = 1 \times 10^8$ dyn-s/cm⁴

is on the upper end (Secomb et al., 1998). The osmotic pressure differences of 20 and 200 dyn/cm² correspond to lower and upper physiological range estimates from (Pries et al., 2000). These values corresponded to an osmotic pressure difference of less than 1% and were obtained by considering reproducing red blood cell exclusion experiments where RBCs either fill or are excluded from the outer edges of the vessel lumen, depending on their speed of travel through the vessel.

The initial shape of the red blood cell for every simulation is taken to be a circle with radius 2.66 μm . While the three-dimensional equilibrium shape of a red blood cell is a biconcave disc, red blood cells become highly deformed in small capillaries and their cross sections take on multiple different shapes *in vivo*. Rather than choosing one of those arbitrary shapes and potentially biasing results, a circular shape was used. Such shapes quickly evolve into more realistic red blood cell cross sections as dynamics proceed (Figure 5). This is especially true since the reference perimeter $nl_0 = 19.4$ μm is chosen to be larger than the initial circular diameter of $2 \cdot \pi \cdot 2.66 = 16.7$ μm , which encourages cells to develop concave shapes like those seen *in vivo*. The center of the initial circular cell is placed in the fluid at location $(x, y) = (-15 \mu\text{m}, y_0)$ where y_0 is in the interval $[y_b, y_t] = [-1.29, 1.29]$. This corresponds to the initial cell shape being at least 0.05 μm away from the middle of the ESL's diffuse boundary (1.05 μm away from the vessel wall). For consistent comparisons, the same interval is used when $\kappa = 0$ and $\kappa = \infty$.

2.4 Analysis of Partitioning, Deformation, and Penetration

To estimate cell partitioning behavior, we follow Barber et al. (2008). To better understand how we determined cell behavior, it is useful to note that background fluid streamlines are streamlines for the flow that occur when the cell is not present. A red blood cell is determined to have entered a specific daughter branch if all three of the following criteria are met simultaneously:

1. it is within $0.1 \mu\text{m}$ of the far vessel wall when no ESL is present or has crossed through the middle of the ESL's diffuse boundary (i.e. is within $1 \mu\text{m}$ of the vessel wall) at any point of its trajectory;
2. all of its nodal velocities point towards that daughter branch (the nodal vertical velocities are either all negative or all positive);
3. the y -value of the cell's centroid lies on the side of the separating background fluid streamline corresponding to that branch.

An example of these criteria applied to a particular simulation is shown in Figure 3. In some cases, these criteria were not met due to a numerical failure (e.g. mesh generation or time stepping failures) and the simulation stopped before a determination had been made. However, every simulation was examined by hand to confirm or determine which daughter branch the cell entered. There were no cases where a determination could not be made.

The fraction of red blood cells fluxing into the top or first daughter branch, Φ_1 , can be estimated for a prescribed flow split, Ψ_1 , using (Barber et al., 2008):

$$\Phi_1(\Psi_1) = \frac{\int_{y_b}^{y_t} p_1(y_0)u_d(y_0)b_1(\Psi_1, y_0)dy_0}{\int_{y_b}^{y_t} p_1(y_0)u_d(y_0)dy_0}. \quad (20)$$

$p_1(y_0)$ is a probability density function describing the probability that the center of a cell passes through the y -value y_0 when the center of the cell passes through $x = x_0 = -15 \mu\text{m}$, $u_d(y_0)$ is the estimated speed at which cells pass through $x = x_0$ when their center passes through y_0 , and $b_1(\Psi_1, y)$ is a piecewise function defined as 1 if the cell initialized at (x_0, y_0) enters the top daughter branch and 0 otherwise. $p_1(y_0)$ is assumed to be a uniform probability density function, as in Barber et al. (2008). $u_d(y_0)$ is the quartic function of y_0 that best fits (in the sense of least squares) estimates of cell velocities obtained from nine circular cells placed at $x_0 = -15 \mu\text{m}$ and at nine different y_0 values evenly distributed across the interval $[y_b, y_t]$. $b_1(\Psi_1, y)$ is estimated by finding the initial y -value y_c above which a cell will enter the top branch and below which the cell will enter the bottom branch. y_c is found using a

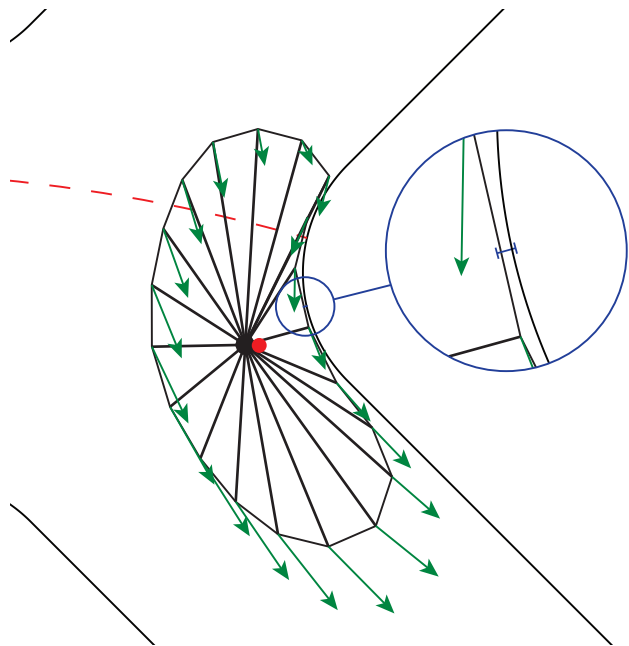


Fig. 3 Illustration of the three branching criteria, all three of which must be satisfied to determine that a red blood cell has entered a specific daughter branch. The blue, green, and red components of the figure correspond to the first, second, and third criteria listed in the text. The green arrows are the nodal velocities, the blue inset highlights the cell distance to the wall, the red dashed line represents the separating background fluid streamline, and the red dot is the centroid of the cell

bisection algorithm that iterates until y_c is bounded by a $0.041 \mu\text{m}$ wide interval and then returns the average of its upper and lower bound as its estimate for y_c .

We also investigate how varying the ESL hydraulic resistivity and osmotic pressure difference can affect red blood cell deformation in diverging microvessel bifurcations. To do so, we calculate the fractional shape disagreement between two simulated cells initialized at the same location, y_0 , by using the equation:

$$SD(y_0, d_c) = 1 - \frac{\text{overlapping cell area}}{\text{average cell area}}. \quad (21)$$

$SD(y_0, d_c)$ is a function of a common distance travelled by the centroids of both cell membranes, d_c . A similar equation was employed by Barber and Zhu (2019) in regards to the deformation of cancer cells in a microfluidic channel. Higher values of κ will produce more centralized flow profiles and faster traveling red blood cells. To better isolate effects due to deformation vs translation, we compare the shapes of cells that have traveled the same distance instead of the same time.

Because an adaptive time-stepper is used, the discrete times and distances at which cell shapes are calculated are not necessarily the same across different simulations. To find the shape of each compared cell

after it has traveled d_c μm , we use linear interpolation with respect to the distance travelled by its cell centroid. The shape disagreement at d_c μm can then be calculated using the formula above. In addition, we can calculate an ‘‘average shape disagreement’’ between different $(\kappa, \Delta\pi_p)$ sets by averaging with respect to initial cell displacement and distance traveled (0 to 30 μm):

$$\overline{SD} = \int_{-1.29}^{1.29} \int_0^{30} S_D(y_0, d_c) dd_c dy_0 / (2 \cdot 1.29 \cdot 30). \quad (22)$$

High sensitivity of results to a particular parameter (κ or $\Delta\pi_p$) will correspond to a high percentage disagreement between cell membrane shapes, as this indicates a large differential effect on deformation of the cell.

Finally, we consider how much the red blood cells invade or penetrate the ESL region. This is measured at any given time, t , for a cell that initially started at y_0 by calculating the penetration of the red blood cell, δ , into the ESL region at that time as follows:

$$\delta(t, y_0) = w - \min_{s_B, s_C} \|\mathbf{B}(s_B) - \mathbf{C}(s_C)\|_2. \quad (23)$$

$\mathbf{B}(s_B)$ is a parametrization of the boundary curve corresponding to the vessel wall and $\mathbf{C}(s_C)$ is a parametrization of the cell membrane curve that travels through the nodes and along the external viscoelastic elements. This produces a positive value for red blood cells penetrating past the middle of the ESL’s diffuse boundary and a negative value for those unable to penetrate past that midpoint. This measure is used to consider how red blood cell penetration of the ESL depends on the initial position of the cell and the distance the cell travels.

To allow general comparison across different $(\kappa, \Delta\pi_p)$ sets for a given flow split, we define ‘‘average passing time’’, \bar{t}_p , and ‘‘average maximum penetration distance’’, $\bar{\delta}_{max}$. Passing time, t_p , is a function of cell initial position, y_0 , and is defined as the time it takes for cells to travel 30 μm . This is approximately the time necessary to fully navigate the bifurcation and be successfully partitioned. Average passing time is given by:

$$\bar{t}_p = \int_{-1.29}^{1.29} t_p(y_0) dy_0 / (2 \cdot 1.29). \quad (24)$$

The maximum penetration distance, δ_{max} , for a given initial cell position, y_0 , is found by taking the maximum of the penetration distance, δ , over the entire simulation time: $\delta_{max}(y_0) = \max_t(\delta(t, y_0))$. The average maximum penetration distance is found by averaging over y_0 the maximum penetration distance for all cells that significantly penetrate the ESL, which corresponds to cells where $\delta > 0$:

$$\bar{\delta}_{max} = \frac{\int_{-1.29}^{1.29} \delta_{max}(y_0) H(\delta_{max}(y_0)) dy_0}{\int_{-1.29}^{1.29} H(\delta_{max}(y_0)) dy_0}. \quad (25)$$

$H(x)$ is the Heaviside function that is 0 when $x < 0$ and 1 otherwise.

3 Results

Results suggest that variations in the hydraulic resistivity and osmotic pressure difference produce relatively little variation in terms of red blood cell partitioning. Despite this, relatively large variations in red blood cell deformation and penetration of the ESL can still result when ESL properties are varied.

3.1 Flow resistance comparison

To better validate the model, we considered a cell in a 6 μm wide channel of length 40 μm that includes a 1 μm wide ESL on either side of the channel. As done for the bifurcation, the inlet pressure and normal derivatives are set to zero while the outlet normal derivative and velocity are prescribed (see Section 2). By assuming a subset of the domain from $x = -L_H/2$ to $L_H/2$ (cell centered at $x = 0$) was similar to a periodic scenario, we were able to estimate the flow resistance in the system for the hematocrit consistent with 1 RBC per L_H units of tube. The cell shapes agreed well with those predicted in Secomb et al. (1998) (included an ESL) and the flow resistances agreed well with the *in vivo* estimates in Pries et al. (1994). In particular, for an estimated discharge hematocrit of 45%, our flow resistance estimate was within 20% of the experimental estimate.

3.2 Partitioning Behavior Dependence on ESL Properties

Varying hydraulic resistivity and osmotic pressure difference result in only minor changes in red blood cell partitioning. Figure 4a shows the predicted y_c as a function of the fraction of bulk blood flow entering the top daughter branch, Ψ_1 . y_c is the critical initial y -value of the red blood cell center above which the cell would enter the top branch and below which the cell would enter the bottom branch. Simulations show that cells are much more likely in general to enter a high flow branch, consistent with experimental trends. Using Equation (20) produces Figure 4b showing the estimated fraction of red blood cells entering the top branch, Φ_1 , as a function of the bulk blood flow entering that branch, Ψ_1 . In this panel as well, the model produced plots are compared to the empirically derived function from Pries and Secomb (2005).

The blue solid lines correspond to a high hydraulic resistivity of $\kappa = 10^8$ dyn·s/cm⁴ and a high osmotic pressure difference of $\Delta\pi_p = 200$ dyn/cm². Using a low osmotic pressure difference of $\Delta\pi_p = 20$ dyn/cm² produces an identical curve (not shown) suggesting that the osmotic pressure difference does not significantly affect partitioning when the hydraulic resistivity is high. Lowering the hydraulic resistivity to the low pathological value of $\kappa = 10^6$ dyn·s/cm⁴ while maintaining a high osmotic pressure difference produces the red solid lines and a change in partitioning behavior is seen. To understand this change in behavior, we first note that uniform partitioning corresponds to the straight diagonal line $\Phi_1 = \Psi_1$. That is, uniform partitioning happens when the fraction of red blood cells entering the top branch equals the fraction of bulk blood entering that branch. The red curves are farther away from that straight line than the blue curves suggesting that lowering hydraulic resistivity results in more nonuniform partitioning. Lowering the osmotic pressure difference produces the red dashed curves. This further increases the nonuniformity of the partitioning. These changes in partitioning, however, are smaller compared to other factors that can affect partitioning behavior such as red blood cell flexibility and vessel size. For example, at a flow split of 37.5%, lowering the values of hydraulic resistivity and osmotic pressure difference decreased the fraction of red blood cells entering the low flow branch by approximately 11%. However, comparing the partitioning of rigid cells to flexible ones produces a decrease of around 36% (Barber et al., 2008), while increasing a vessel diameter from 8 μm to 10 μm produces an increase of 16% (Pries and Secomb, 2005).

To better understand why changing ESL properties can affect partitioning behavior, we investigated differences in general dynamics experienced by cells that are partitioned differently because of ESL property differences. Figure 5 shows a typical comparison by plotting results from two separate simulations on the same plot. Also included are cell streamlines for each cell that show the paths that the centroids of the cells followed. The simulations have the same flow split of 31.25% into the top branch, high osmotic pressure difference of 200 dyn/cm², and initial cell location, $((x_0, y_0) = (-15, 1.048))$. The hydraulic resistivity in one simulation uses $\kappa = 10^8$ dyn·s/cm⁴ (blue) while $\kappa = 10^6$ dyn·s/cm⁴ (red) is used in the other simulation. Figure 5a shows the cells after they have traveled 0, 10, 20, and 30 μm . The cell with the more resistive ESL (blue) elongates/deforms more than the other cell early on (e.g. compare cell shapes after 10 μm). Due to this, the blue deformed cell migrates more towards the mother vessel centerline than its partner. In fact, the blue cell

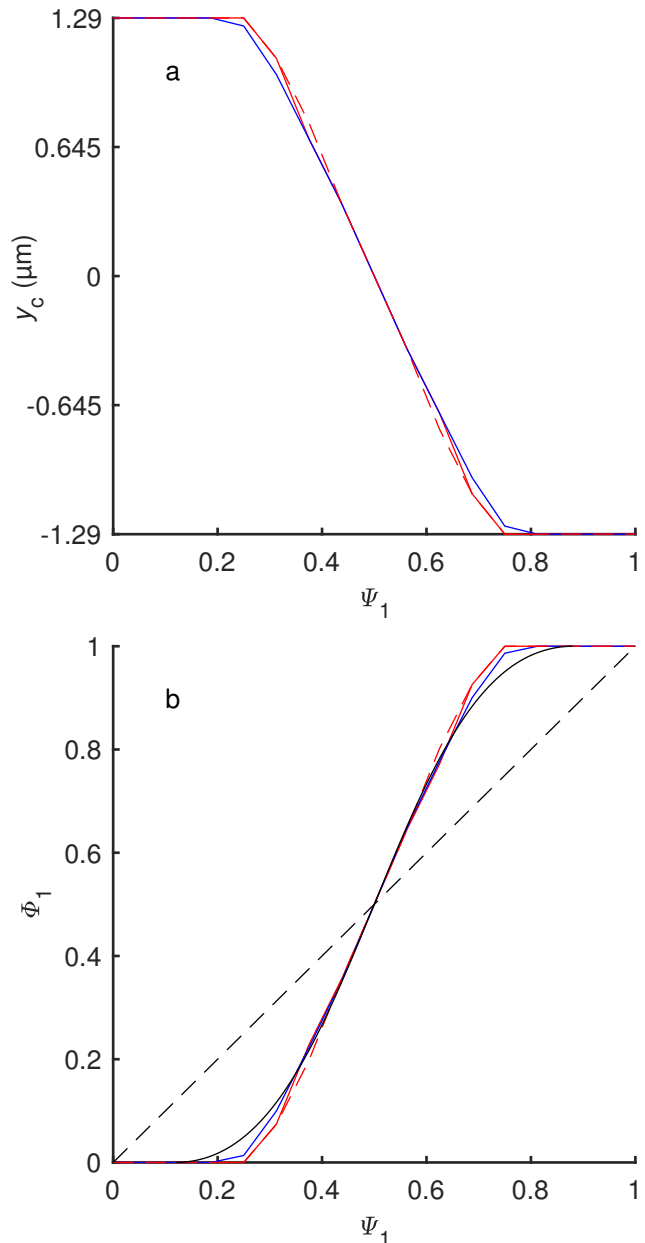


Fig. 4 The effects of ESL properties on red blood cell partitioning at a bifurcation. **a** The critical initial y -value of the red blood cell center, $y_c(\Psi_1)$, and **b**, the fraction of red blood cells entering the top branch, $\Phi_1(\Psi_1)$, as a function of bulk blood entering the top branch, Ψ_1 . The results are shown for three sets of hydraulic resistivity, κ , and osmotic pressure difference, $\Delta\pi_p$, values: $(\kappa, \Delta\pi_p) = (10^8 \text{ dyn}\cdot\text{s}/\text{cm}^4, 200 \text{ dyn}/\text{cm}^2)$ (blue), $(\kappa, \Delta\pi_p) = (10^6 \text{ dyn}\cdot\text{s}/\text{cm}^4, 200 \text{ dyn}/\text{cm}^2)$ (red), and $(\kappa, \Delta\pi_p) = (10^6 \text{ dyn}\cdot\text{s}/\text{cm}^4, 20 \text{ dyn}/\text{cm}^2)$ (red dashed). Uniform partitioning is represented by the line $\Psi_1 = \Phi_1$ (black dashed). The solid black curve is the experimental estimate from Pries and Secomb (2005). Lowering the hydraulic resistivity and the osmotic pressure results in more nonuniform partitioning

streamline remains below the red cell streamline until both cells have traveled approximately $17.9 \mu\text{m}$. After that, the blue cell streamline crosses over the red cell streamline and the blue cell enters the top branch while the red enters the bottom branch.

To better understand the cell streamline crossover, we more closely investigate the velocities of the fluid and nodes on the cells in Figure 5b and c. Increasing the resistivity results in a significantly more centralized flow field. This leads to higher shear rates and more red blood cell deformation upstream of the vessel, as previously noted. More importantly, however, it enhances the cell obstruction effect (see section 4.4 for a discussion on possible boundary condition effects). In the cell obstruction effect (Barber et al., 2008), when a cell blocks a downstream vessel it is more likely to get pulled into that branch. This is because of volume conservation; by entering the obstructed branch, the cell helps conserve the downstream volume flux/flow split. A similar effect can be felt when initially pulling a plug from a drain. The harder it is for fluid to bypass the cell when entering the obstructed branch, the stronger the obstruction effect will be. The high hydraulic resistivity effectively narrows the gap between obstructed cells and the vessel wall making the obstruction effect stronger and more likely to pull cells into the obstructed branch.

The obstruction effect typically alters partitioning behavior by pulling cells near the low flow branch into that branch. To understand why, one can define a separating cell streamline that starts at y_c , travels to the right towards the bifurcation, and separates cells entering the top branch from those entering the bottom branch (black dashed line in Figure 7b). When more flow enters one branch compared to the other, the separating cell streamline will be closer to the low flow branch than to the high flow branch, corresponding to fewer cells on the low flow side entering the low flow branch and more cells on the high flow side entering the high flow branch. Cells near this streamline are the cells whose partitioning behavior can be most easily altered by various perturbations. Cells near this streamline are also closer to the low flow branch, more likely to obstruct the low flow branch, and more likely to have the obstruction effect pull them into the low flow branch. See (Barber et al., 2008; Barber, 2009) for more detailed discussions.

Higher hydraulic resistivity enhances cell migration towards the center of the vessel upstream of the bifurcation, which encourages cells to enter high flow branches even more than usual and encourages more nonuniform partitioning. The higher hydraulic resistivity, however, also enhances the obstruction effect, which encourages

cells to enter low flow branches and encourages more uniform partitioning. Ultimately, the obstruction effect is stronger so that raising the hydraulic resistivity produces more uniform partitioning, as seen in Figure 4.

When the osmotic pressure difference is decreased ($200 \rightarrow 20 \text{ dyn/cm}^2$) while the hydraulic resistivity is kept low ($10^6 \text{ dyn}\cdot\text{s/cm}^4$), upstream of the bifurcation the cells remain relatively far from the ESL so that the forces on the cell due to the osmotic pressure difference remain negligible. Hence the osmotic pressure difference has a negligible effect on cell migration upstream of the bifurcation. At the bifurcation, however, if both the osmotic pressure difference and hydraulic resistivity are low, the cell can significantly penetrate the ESL. When cells sink into the ESL, they reduce the amount that they obstruct the downstream branches (see Figure 8a), which weakens the obstruction effect and produces more nonuniform partitioning. ESL penetration is discussed in more detail in 3.5.

3.3 ESL Hydraulic Resistivity's Effects on Deformation and Motion

Figure 6 compares simulations using two different hydraulic resistivities, $\kappa = 10^8 \text{ dyn}\cdot\text{s/cm}^4$ (blue) and $\kappa = 10^6 \text{ dyn}\cdot\text{s/cm}^4$ (red), when the osmotic pressure difference is held at 200 dyn/cm^2 and 37.5% of the flow enters the top branch. Initial cell centers are started at $y_0 = 0.726 \mu\text{m}$ (Figure 6a and c) and at $y_0 = 0.645 \mu\text{m}$ (Figure 6b and d). These locations were chosen so that they are close to, approximately equidistant from, and above and below the predicted critical value, $y_c = 0.685 \mu\text{m}$ (same critical value for both resistivities). At $y_0 = 0.726 \mu\text{m}$ above the center line, both cells enter the top, low flow daughter branch, and at $y_0 = 0.645 \mu\text{m}$ above the center line, both cells enter the bottom, high flow daughter branch. The trajectories of the centroid of each cell are also plotted. In general, cells in the higher hydraulic resistivity cases appear to elongate and deform more before, during, and after partitioning. The cell shapes produced by our model (e.g. Figure 6b) agree with those seen *in vivo* such as those found in Pries and Secomb (2008), in a similar fashion to the agreement seen in Barber et al. (2008).

In Figure 6c, shape disagreements between the high and low hydraulic resistivity cases from Figure 6a (solid) and b (dashed) are plotted over the total distance traveled by the cells. The cells entering the bottom, high flow daughter branch see a larger shape disagreement as they pass through the bifurcation than those entering the top, low flow daughter branch. However, before the cells interact with the ESL at the bifurcation, the reverse is true. Figure 6d compares the total time a cell

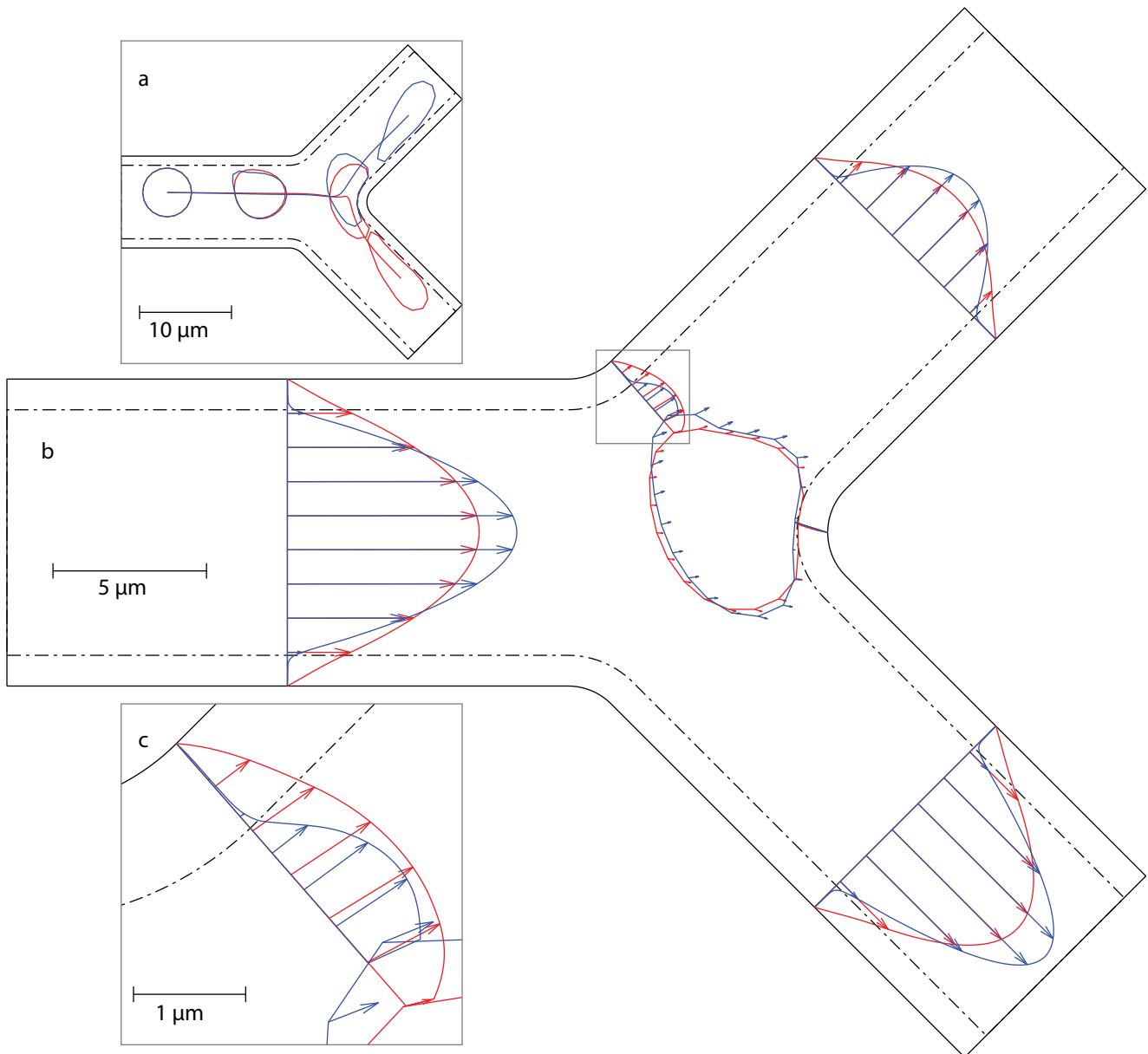


Fig. 5 Example of different partitioning behaviors for cells with differing hydraulic resistivities. Blue represents the high hydraulic resistivity simulation of $\kappa = 10^8$ dyn-s/cm⁴, and red represents the low hydraulic resistivity simulation of $\kappa = 10^6$ dyn-s/cm⁴. 31.25% of the flow exits out the top branch and the osmotic pressure difference is 200 dyn/cm². **a** Snapshots of red blood cells after they have traveled 0, 10, 20, and 30 μm . **b** Velocity profiles of the bulk blood flow, as well as nodal velocities of the red blood cells after travelling 18.5 μm . The region enclosed in the grey box is shown in **c**. **c** Velocity profiles of the bulk blood flow at the mouth of the low flow daughter branch from the cell membrane to the vessel wall, including the ESL

is traveling through the bifurcation and the total distance the cell travels for each simulation. As before, blue corresponds to the high hydraulic resistivity, red to the low hydraulic resistivity, solid to $y_0 = 0.726$ μm (low flow branch cells), and dashed to $y_0 = 0.645$ μm (high flow branch cells). The cells in the higher hydraulic resistivity cases travel faster because the flow is faster in the vessel center (Figure 5b). Cells entering the high flow branch travel faster, which makes sense because the flow is, in fact, higher near and in that branch.

Flow centralization in the higher resistivity cases also helps explain the higher deformation at the bifurcation. In higher resistivity scenarios, as before (Figure 5c), fluid is effectively forced through narrower gaps between the cell and the vessel wall. This yields higher shear rates as fluid squeezes through those gaps, and higher forces allowing the fluid to stretch and compress the cell further than in lower resistance scenarios.

Figure 7a shows how differences in deformation due to differences in hydraulic resistivity depend on the cell

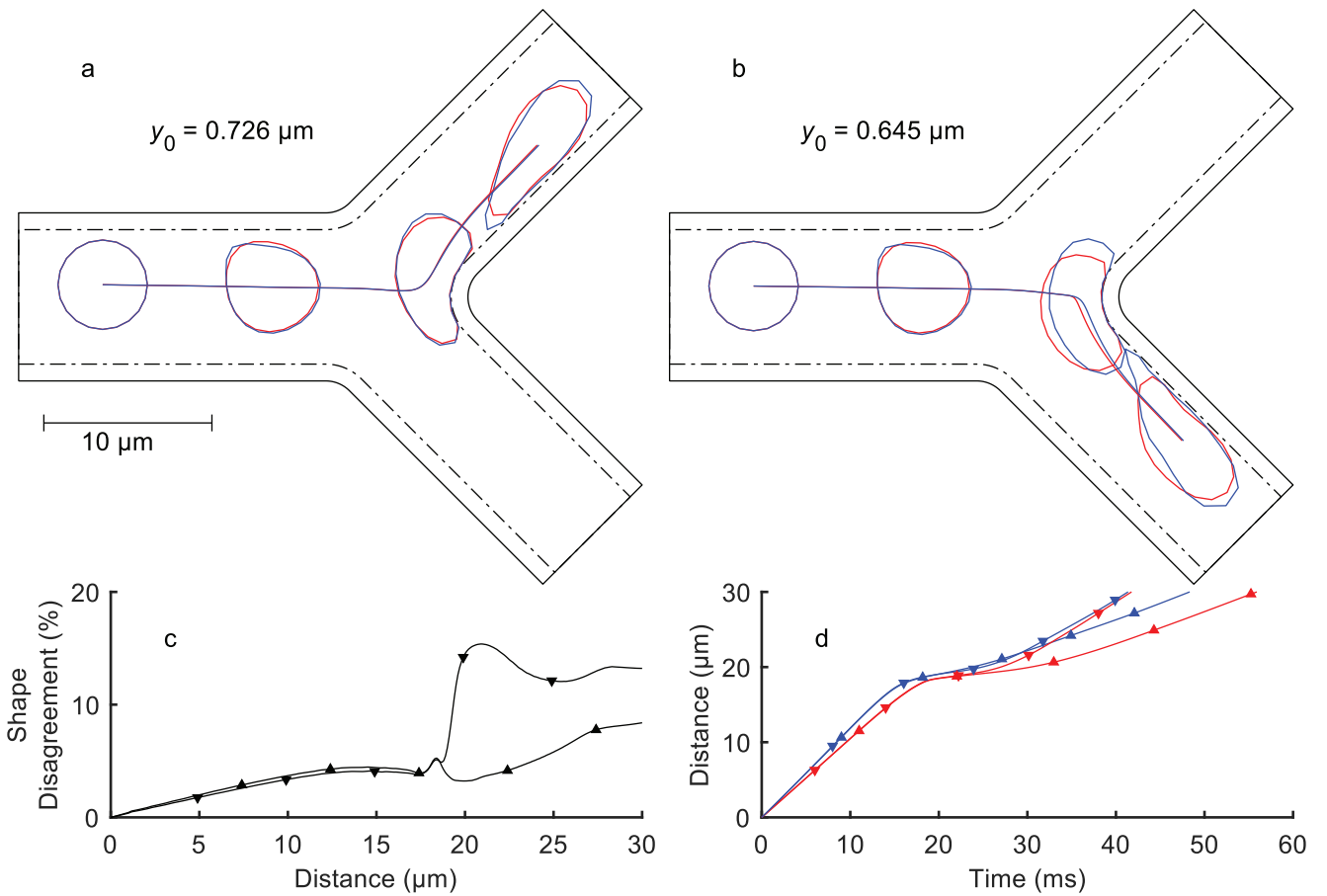


Fig. 6 The effects of hydraulic resistivity in the ESL on cell shape and speed. Blue corresponds to $\kappa = 10^8 \text{ dyn}\cdot\text{s}/\text{cm}^4$ and red to $\kappa = 10^6 \text{ dyn}\cdot\text{s}/\text{cm}^4$. Cell shapes after each cell has traveled 0, 10, 20, and 30 μm are placed on the same plot in **a** ($y_0 = 0.726$) and **b** ($y_0 = 0.645$). 37.5% of the flow enters the top branch and an osmotic pressure difference of $200 \text{ dyn}/\text{cm}^2$ is used. The trajectories of the centroids of the cells are also plotted. **c** Shape disagreement percentages between the cells in panel a (symbols pointing up) and between the cells in panel b (symbols pointing down) showing the effects of varying hydraulic resistivity. **d** Distance traveled by the cell as a function of the time spent traversing the bifurcation

position upstream of the vessel bifurcation (y_0) and how far the cells travel. The plot uses all viable initial cell center locations ($y_0 \in [-1.29, 1.29]$), 37.5% flow into the top branch, and the higher osmotic pressure difference, $200 \text{ dyn}/\text{cm}^2$. After cells have travelled $10 \mu\text{m}$ (red in Figure 7b), before encountering the bifurcation, the shape disagreement is highest near the walls (where the shear rate is higher, in general) and lower near the vessel center. At $20 \mu\text{m}$, cells begin to interact with the far wall of the bifurcation and an additional spike in shape disagreements immediately below $y_0 = y_c$ (black dashed line) develops. The value of y_c is predicted to be the same for each level of hydraulic resistivity considered here (see Table 5). At that location, cells differentially interact with the ESL with cells in the higher hydraulic resistivity cases stretching out more than their cohorts as in Figure 6b. No similar spike is seen above the predicted critical value. At $30 \mu\text{m}$, after cells have been partitioned, the shape disagreements increase further

with the exception of the spike just below the critical value that decreases slightly. Figure 7b was included to show the average cell center locations for the cells in the compared high and low hydraulic resistivity scenarios after they had traveled 0, 10, 20, and 30 μm . The panel additionally shows a slight constriction of cell center trajectories due to cell migration before the cell distributions widen farther downstream.

For the flow split $\Psi_1 = 0.375$, Tables 3 and 4 give the average shape disagreement percentages for a range of hydraulic resistances at low and high osmotic pressures, respectively. As seen in Table 4, the scenarios considered in Figure 7 have a corresponding average shape disagreement of 9.06%. In general, comparing more disparate levels of hydraulic resistivity leads to a higher shape disagreement percentage, regardless of osmotic pressure difference. Also, lower osmotic pressure differences lead to higher shape disagreement percentages. The special cases for a vessel without an ESL

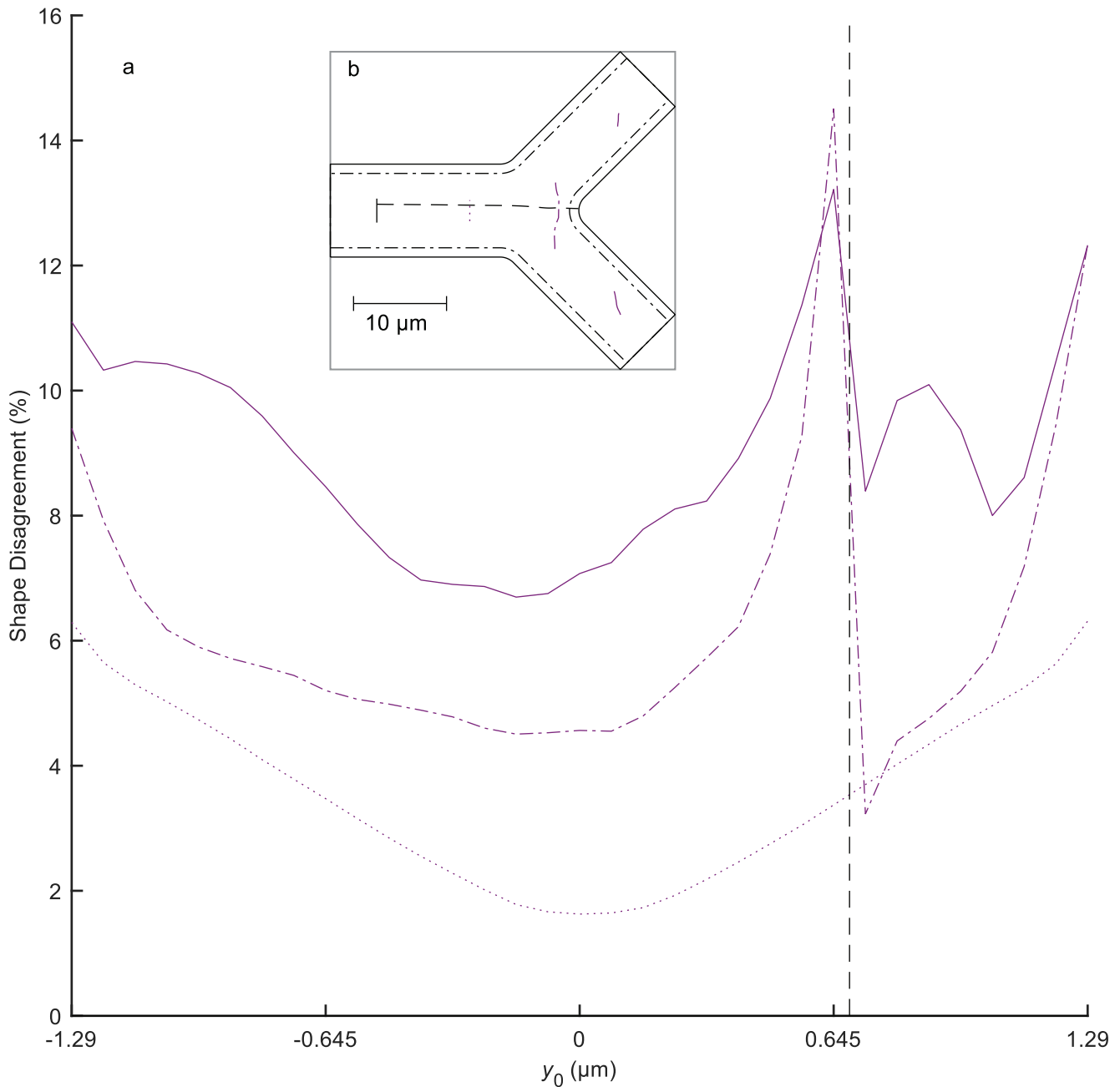


Fig. 7 Cell shape disagreement increases with distance and when near walls or on the high flow side of the separating cell streamline. Cells are compared after traveling 0 (black), 10 (dotted), 20 (dot-dashed), and 30 (solid) μm . 37.5% of the flow enters the top branch and the osmotic pressure difference is held at 200 dyn/cm^2 . **a** Cell shape disagreement percentage between cells for the high ($\kappa = 10^8 \text{ dyn-s/cm}^4$) and low ($\kappa = 10^6 \text{ dyn-s/cm}^4$) hydraulic resistance cases as a function of cell starting position y_0 . The black dashed vertical line is located at the critical initial cell center y -value of $y_c = 0.685$. **b** The cell center locations after they have traveled 0, 10, 20, and 30 μm . The black dashed curve is the predicted average separating cell streamline that begins at the critical initial cell center location

($\kappa = 0, \Delta\pi_p = 0$) and a vessel with an impenetrable ESL ($\kappa = \infty, \Delta\pi_p = \infty$) were included to allow for comparison between the physiological cases and these more extreme cases. The variation amongst the physiological cases is of the same order as the variation found when including the extreme cases suggesting that pathologies

associated with missing or heavily damaged ESLs may also be experienced to a lesser but still significant extent by individuals with less damaged ESLs.

Table 3 Average shape disagreement percentages when comparing simulations with different hydraulic resistivities, a low osmotic pressure difference of $\Delta\pi_p = 20 \text{ dyn/cm}^2$ (unless otherwise listed), and a flow split of $\Psi_1 = 0.375$

$\kappa \text{ (dyn}\cdot\text{s/cm}^4\text{)}$	$0, \Delta\pi_p = 0$	10^6	10^7	10^8
$\infty, \Delta\pi_p = \infty$	20.35	14.20	10.02	4.11
10^8	17.72	11.52	6.70	
10^7	13.21	5.88		
10^6	8.77			

Table 4 Average shape disagreement percentage when comparing simulations with different hydraulic resistivities, a high osmotic pressure of $\Delta\pi_p = 200 \text{ dyn/cm}^2$ (unless otherwise listed), and a flow split of $\Psi_1 = 0.375$

$\kappa \text{ (dyn}\cdot\text{s/cm}^4\text{)}$	$0, \Delta\pi_p = 0$	10^6	10^7	10^8
$\infty, \Delta\pi_p = \infty$	20.35	10.31	7.43	3.23
10^8	18.06	9.06	5.62	
10^7	15.37	4.29		
10^6	14.17			

3.4 ESL Osmotic Pressure Difference's Effects on Deformation and Motion

Figure 8 compares simulations using two different osmotic pressure differences, $\Delta\pi_p = 200 \text{ dyn/cm}^2$ (blue) and 20 dyn/cm^2 (red), when the hydraulic resistivity is held at $10^6 \text{ dyn}\cdot\text{s/cm}^4$ (solid) and $10^8 \text{ dyn}\cdot\text{s/cm}^4$ (dashed) and 37.5% of the flow enters the top branch. As seen in Figures 6 and 7, comparisons of cells near and below the centerline tend to result in larger percentage disagreements than comparisons of cells near and above the centerline. Focusing on the larger percentage disagreements, the cell centers in Figure 8 were started at $y_0 = 0.645$ and were chosen so that they are close to and below the predicted critical values, $y_c = 0.685 \mu\text{m}$ ($\Delta\pi_p = 200 \text{ dyn/cm}^2$) and $0.766 \mu\text{m}$ ($\Delta\pi_p = 20 \text{ dyn/cm}^2$). The trajectories of the cell centroids are also plotted.

Before partitioning and upstream of the bifurcation, the deformation of the cells are very similar. This is because the cells remain far from the wall where the forces due to osmotic pressure differences are quite small. In addition, the background flow field is exactly the same for the two simulations as that flow field depends on hydraulic resistivity but not on osmotic pressure differences. At the bifurcation in Figure 8a, the cell in the lower osmotic pressure difference scenario penetrates the ESL significantly more than its peer. While the majority of the shape disagreement is due to this penetration difference, the red cell is, in fact, slightly rounder than the blue cell. This can be measured using round-

ness defined as the area of the shape divided by the area of a circle with the same perimeter as the shape; 100% corresponds to a circular shape while 0% corresponds to a flat shape with 0 area. The roundness of the red cell is 88.7% while that of the blue cell is 79.9%. After the bifurcation, the blue cell becomes slightly rounder/less elongated (76.2% vs 75.7%). This is because it takes more time for the red cell to return from its ESL incursion. During that longer time period the red cell is subjected to higher shear rates in the region that cause it to elongate more than its partner. Similar dynamics can be seen for high hydraulic resistivity (Figure 8b) though they are significantly diminished compared to the low hydraulic resistivity case.

Figure 8c shows the percentage shape disagreement between the two different osmotic pressure differences (200 and 20 dyn/cm^2) for both the low hydraulic resistivity case (solid) and the high hydraulic resistivity case (dashed). Shape disagreement is practically 0 until the cells get closer to the far wall. At that point, shape disagreement increases as they negotiate the far wall/ESL of the bifurcation and then decreases after that negotiation is complete. While the higher hydraulic resistivity has lower deformation differences, the differences are still appreciable compared to the low hydraulic resistivity case. Figure 8d shows the distance traveled by the four cells. The higher hydraulic resistivity cases (dashed) travel faster than their lower hydraulic resistivity counterparts (solid). Focusing on just the lower hydraulic resistivity cases, it can be seen that the cells in the low osmotic pressure difference case (red) travel faster as they sink into the ESL but then slower as they withdraw from the layer. While it is more difficult to see and much more subdued, the same trend occurs for the higher hydraulic resistivity case.

3.5 Cell Penetration in the ESL

Plotted against the entire range of possible initial cell center locations (y_0) for 37.5% of the flow entering the top branch, Figure 9a shows the maximum distance a cell penetrates into the ESL for low ($10^6 \text{ dyn}\cdot\text{s/cm}^4$; blue), medium ($10^7 \text{ dyn}\cdot\text{s/cm}^4$; green), and high ($10^8 \text{ dyn}\cdot\text{s/cm}^4$; red) hydraulic resistivities at both low (20 dyn/cm^2 ; dashed) and high (200 dyn/cm^2 ; solid) osmotic pressure differences. As expected, the closer cells are to the separating cell streamline/ y_c , the farther the cells penetrate into the ESL. At the same time, over fifty percent of the cells in the low osmotic pressure difference scenarios penetrate beyond the ESL diffuse boundary midpoint suggesting that close proximity to the separating cell streamline is not a requirement for significant penetration of the ESL. In general, lower

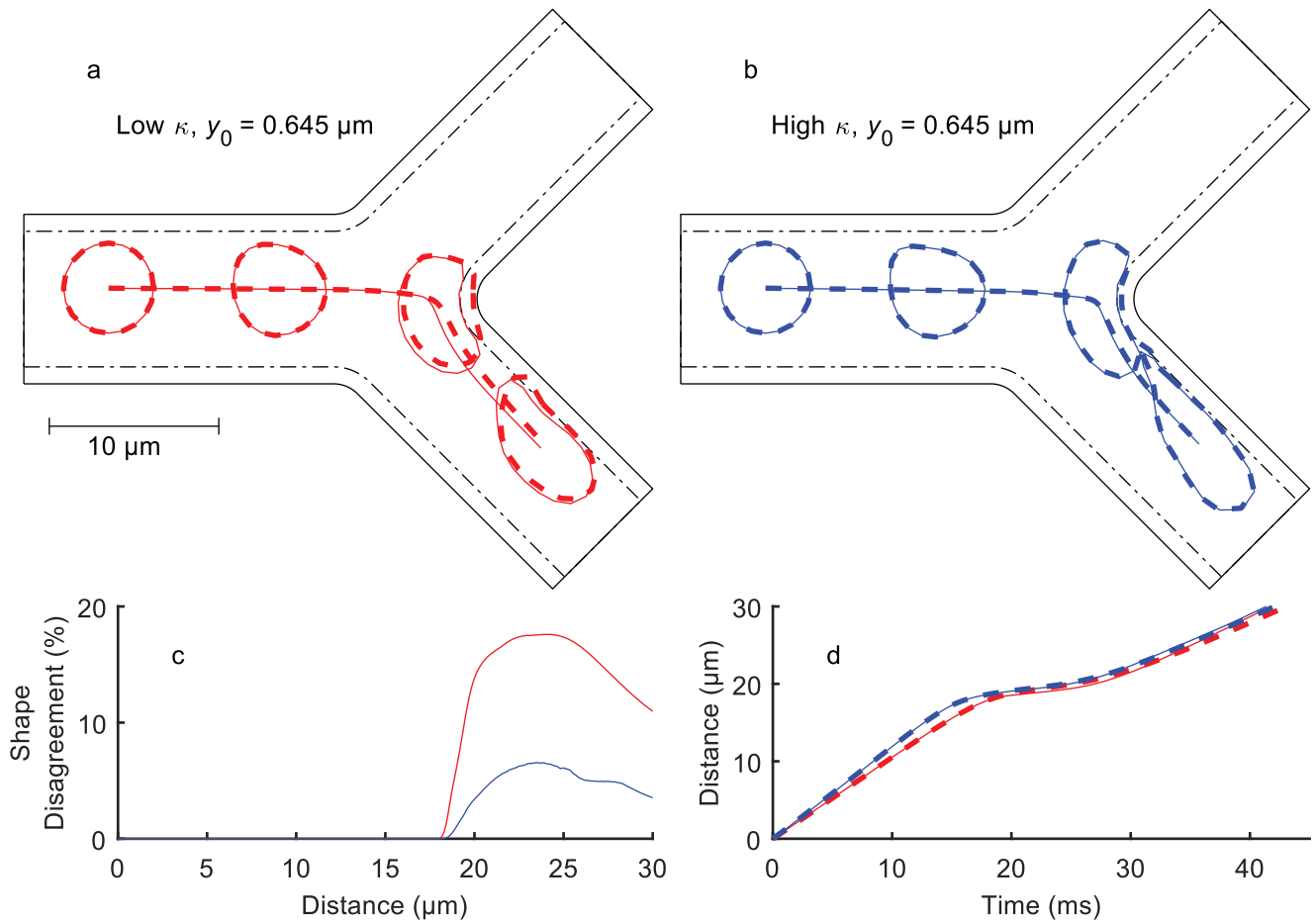


Fig. 8 The effects of osmotic pressure difference in the ESL on cell shape and speed. Solid curves represent high osmotic pressure difference simulations using $\Delta\pi_p = 200 \text{ dyn/cm}^2$ and dashed curves represent low osmotic pressure difference simulations using $\Delta\pi_p = 20 \text{ dyn/cm}^2$. All cells begin at $y_0 = 0.645 \mu\text{m}$ and 37.5% of the bulk flow enters the top branch. Cell shapes after each cell has traveled 0, 10, 20, and 30 μm are placed on the same plot and are shown for **a** two low hydraulic resistivity cases ($\kappa = 10^6 \text{ dyn}\cdot\text{s/cm}^4$) and **b** two high hydraulic resistivity cases ($\kappa = 10^8 \text{ dyn}\cdot\text{s/cm}^4$). The trajectories of the centroids of the cells are also plotted. **c** Shape disagreement percentage between the cells in panel a (red) and panel b (blue). **d** Distance traveled by the cell as a function of the time spent traversing the bifurcation

hydraulic resistivity and lower osmotic pressure differences result in higher penetration distances of cells into the ESL. Osmotic pressure differences appear to alter penetration more than hydraulic resistivity. Lowering hydraulic resistivity from physiological to pathological values increased maximum penetration distance by two-fold, while lowering osmotic pressure difference increased the same by fifteen-fold. A maximum penetration distance of 3.7% of the width of the ESL (w) is seen for the high osmotic pressure difference and high hydraulic resistivity case while 92.1% is seen for the low osmotic pressure and low hydraulic resistivity case, an increase of thirty-fold.

Figure 9b shows ESL penetration as a function of time for multiple simulations with cells starting at $y_0 = 0.645$ (chosen to be near and below y_c for all six cases). The plot is representative of the behavior seen in simulations where a significant amount of positive penetra-

tion takes place. In the cases with low osmotic pressure difference, penetration is not localized in time, as once a maximum penetration distance is reached by the cell, it tends to remain near that penetration distance for a significant amount of time thereafter. This corresponds to cells sinking into the layer and slowly pulling out as they are partitioned into a downstream branch. For cases of high osmotic pressure difference, the time a cell spends near the maximum penetration distance is shortened as the cells have penetrated the layer much less and take much less time to pull out of the layer.

For the flow split where 37.5% of the flow goes into the top branch, Table 5 gives the average time a cell takes to travel 30 μm /navigate the bifurcation, \bar{t}_p , the average maximum penetration distance into the ESL, $\bar{\delta}_{max}$, and the critical initial cell center y -value, y_c , for hydraulic resistances at both low and high osmotic pres-

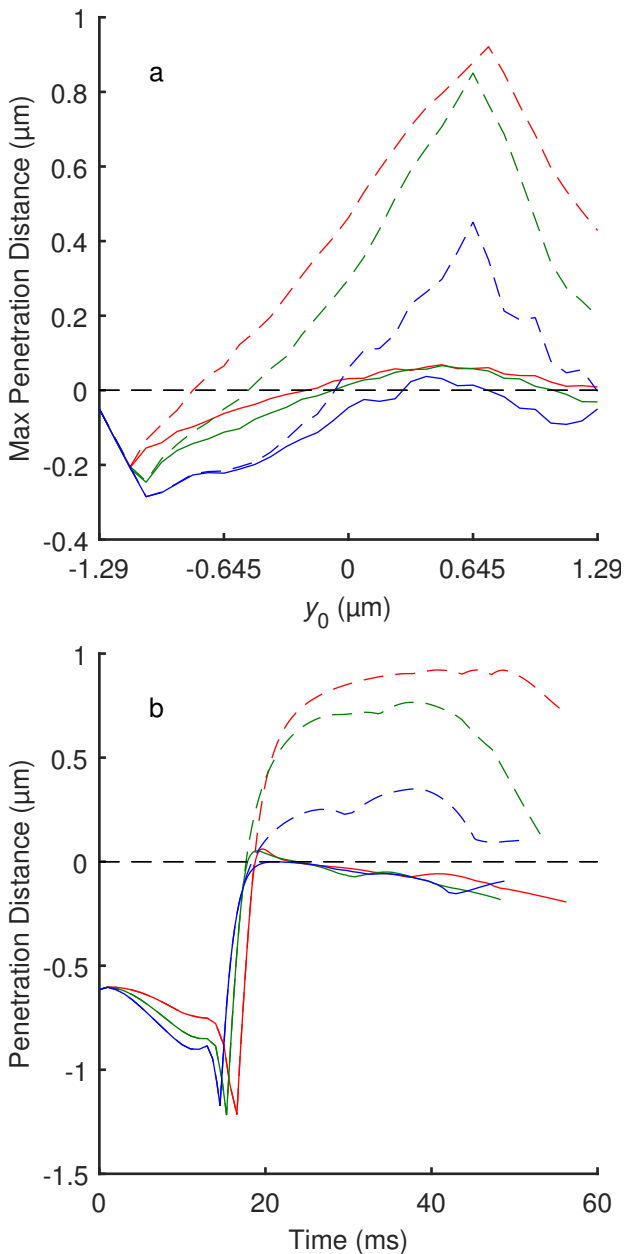


Fig. 9 Cell penetration distance dependence on initial cell position and time when 37.5% of the flow enters the top branch. High ($\kappa = 10^8$ dyn·s/cm⁴; blue), medium (10^7 dyn·s/cm⁴; green), and low (10^6 dyn·s/cm⁴; red) hydraulic resistivity cases are plotted for both high ($\Delta\pi_p = 200$ dyn/cm²; solid) and low ($\Delta\pi_p = 20$ dyn/cm²; dashed) osmotic pressure differences. **a** Maximum penetration distance into the ESL in μm as a function of initial cell center y -values (y_0). **b** Penetration distance into the ESL in μm as a function of time. The initial cell center for all simulations was chosen to be $y_0 = 0.645$, which is near and below y_c for all three cases

Table 5 Average passage times, \bar{t}_p , average maximum penetration distances, $\bar{\delta}_{max}$, and critical y values, y_c for multiple sets of hydraulic resistivity and osmotic pressure difference values when 37.5% of the flow enters the top branch. Results are included for low, medium, and high hydraulic resistivities (10^6 , 10^7 , and 10^8 dyn·s/cm⁴) at both low and high osmotic pressure differences (20 and 200 dyn/cm²; subscripts low and high, respectively). Also included are results for $(\kappa, \Delta\pi_p) = (0,0)$ and (∞, ∞) corresponding to the two extremes of an absent and impenetrable ESL, respectively

κ (dyn·s/cm ⁴)	0 ($\Delta\pi_p = 0$)	10^6	10^7	10^8	∞ ($\Delta\pi_p = 0$)
$\bar{t}_{p,low}$ (ms)	26.43	31.43	29.05	27.43	26.88
$\bar{t}_{p,high}$ (ms)	26.43	30.91	28.70	27.26	26.88
$\bar{\delta}_{max,low}$ (μm)	0	0.526	0.426	0.208	0
$\bar{\delta}_{max,high}$ (μm)	0	0.041	0.039	0.025	0
$y_{c,low}$ (μm)	0.766	0.766	0.685	0.685	0.685
$y_{c,high}$ (μm)	0.766	0.685	0.685	0.685	0.685

sure differences. As before, $(\kappa, \Delta\pi_p) = (0,0)$ and (∞, ∞) are included in order to consider both extremes.

Consistent with observations in previous sections, increasing the hydraulic resistivity lowers the time it takes for the cell to travel through the bifurcation as the centralized flow field speeds up the cells (Figure 5). In addition, increasing the osmotic pressure difference lowers the passage time due to a stiffer ESL that limits cells from sinking far into the ESL. Changing the hydraulic resistivity can have also have a smaller but still significant effect on cell penetration. When the ESL is more porous and the cell approaches the far wall of the bifurcation, the fluid in between that cell and the ESL can escape either along the ESL boundary or through the ESL itself. With this latter additional degree of freedom, cells can more easily and quickly approach and embed themselves in the ESL. They, therefore, sink in deeper and take longer to recover from their ESL incursion. This is especially the case because, as they sink in, they obstruct downstream flow less and therefore experience smaller forces pulling them into downstream vessels. Compared to the no-ESL extremes, cells more slowly pass through bifurcations when an ESL is present.

4 Discussion

Though by a relatively small margin, compared to other factors such as vessel sizes, RBC flexibility, and upstream hematocrit distribution (Barber et al., 2011; Pries and Secomb, 2005; Balogh and Bagchi, 2018), the partitioning behavior of RBCs is influenced by the hydraulic resistivity in the ESL and the difference in the osmotic pressures in the ESL and non-ESL regions. In

particular, increasing the hydraulic resistivity and the osmotic pressure difference results in more uniform partitioning, though the overall change is still very small. The relatively small ESL effect on partitioning is consistent with the findings of microfluidic studies where *in vitro* results (Mantegazza et al., 2020a) agree relatively well with *in vivo* results (Pries and Secomb, 2005) despite the lack of an ESL in the former. In addition, increasing hydraulic resistivity leads to more deformation in general. Increasing the osmotic pressure has little effect on deformation upstream of the bifurcation, decreases deformation as cells sink into the ESL, and increases deformation as cells are pulled out of the ESL. Decreasing the hydraulic resistivity and osmotic pressure differences increases ESL penetration with more penetration resulting when osmotic pressure differences are decreased to lower values compared to when hydraulic resistivities are decreased to lower values.

4.1 Partitioning

When hydraulic resistivity increases, the flow becomes more centralized with higher shear rates in the non-ESL region of the vessel (Figure 5b). This leads to more deformation of RBCs upstream of the bifurcation, which agrees with previous studies (Pfafferoth et al., 1985). More cell deformation leads to a greater rate of cell migration towards the center of the mother vessel and away from the low flow branch, encouraging more nonuniform partitioning wherein the higher flow branch claims even more RBCs than it usually does. However, in this case, the migration effect is not the dominant effect. Higher resistance in the ESL prevents fluid from flowing through the ESL region as quickly, which leads to a cell at the mouth of the low flow daughter branch more completely blocking the flow at that branch when compared to a case with lower resistance in the ESL. This, combined with the more deformed cell shape blocking slightly more of the branch than in the case of lower resistivity, leads to a stronger obstruction effect taking place, which pulls the cell towards the low flow branch and encourages more uniform partitioning. This effect proves stronger in this case than the migration effect. This results in more uniform partitioning in general when hydraulic resistivity increases. However, it is unclear whether such differences will still be observed under less idealized conditions due to the inherently stochastic nature of microcirculatory flows.

As seen in the simulations, osmotic pressure difference has very little effect on flow upstream of the bifurcation. This is not true for flow in the bifurcation region. At lower osmotic pressure differences, the ESL resists compression less allowing the RBCs to sink more deeply

into the ESL as they pass through the bifurcation. This allows such cells to move away from the main flow region and to obstruct vessels less. Therefore, at higher osmotic pressure differences, cells obstruct flow more, which enhances the obstruction effect. This results in more cells being pulled into the low flow instead of the high flow branch and results in more uniform partitioning.

The predicted flow split threshold below which no RBCs enter the low flow branch, which corresponds to the parameter X_0 in Pries' law (Pries et al., 1990), increases (from $X_0 = 0.19$ to 0.25) when decreasing the hydraulic resistivity in the ESL (Figure 4b). This is due to the dominant obstruction effect described above, since a lower hydraulic resistivity level induces weaker obstruction necessitating a higher flow rate before it can pull cells into the low flow branch. Comparing this threshold to the Pries and Secomb (2005) function (black curve) suggests our 2D model typically overestimates the value of this threshold. This trend of overestimation can also be seen by comparing with an experimental study involving $10 \times 8 \mu\text{m}^2$ rectangular channels made of PDMS (polydimethylsiloxane), which have effectively no hydraulic resistivity near the walls (Mantegazza et al., 2020a). There they measured $X_0 = 0.19$ which is less than our low hydraulic resistivity estimate of 0.25. Possible reasons for this overestimation trend are discussed below in study limitations.

The focus of the study is exclusively on the motion of isolated RBCs. By removing the complexity of cell-cell interactions, the influence of the ESL on RBC dynamics may be studied more closely. However, cell-cell interactions have an important impact on RBC partitioning. Initial results from simulations involving an additional RBC suggest that changing ESL parameters, especially hydraulic resistivity, can significantly alter partitioning behavior through multiple mechanisms. For cells entering the bifurcation region in relatively close proximity to each other, leading cells can block following cells from entering the low flow branch. Following cells can also push leading cells into high flow branches (herding effect, Barber et al. (2011)). Both mechanisms reduce the number of cells entering the low flow branch and increase partitioning nonuniformity. However, for larger spacing between cells entering the bifurcation region, the obstruction effect remains the most influential effect, which leads to an overall more uniform partitioning of RBCs. While these preliminary results indicate how ESL parameters may influence cell-cell interactions and thus RBC partitioning, this research is the subject of currently ongoing studies.

4.2 Deformation and Motion

Outside of partitioning effects, the strength of the hydraulic resistivity in the ESL can produce differences in the shape and speed of RBCs. Higher ESL hydraulic resistivity results in greater shear rates in the non-ESL region and higher deformation upstream of the bifurcation (Figure 6a-c). Contact with the ESL at the far wall of the bifurcation however, produces much larger shape disagreements especially when cells travel down the high flow daughter branch. Cells near the separating cell streamline tend to sink into or curve along the ESL. In order to enter one of the branches, such cells must roll along the ESL into that branch. Because the higher flow branch is farther from the separating cell streamline than the low flow branch, cells entering the high flow branch roll for longer. This gives rise to more cell shape disagreement between high flow branch cells when comparing simulations using different ESL properties. This can be seen in Figure 6 and in the spike on the high flow side at 20 and 30 μm in Figure 7. This indicates that greater interaction with the ESL correlates with higher deformation in RBCs. After cells negotiate the bifurcation, shape disagreements in the high flow branch level off slightly, but shape disagreements for both branches remain at significant levels as the cells travel farther down the daughter branches.

Higher hydraulic resistivity in the ESL also results in faster RBCs in bifurcations, as seen in Figure 6d. The curves plotted can be seen to correspond to three different regions, upstream of the bifurcation (less than approximately 20 ms), in the bifurcation region (around 20-25 ms), and downstream of the bifurcation (after approximately 25 ms). Faster speeds before and after the bifurcation in the high hydraulic resistivity case can be explained by greater fluid velocity in the free flowing regions that compensates for the lower fluid velocity in the ESL regions. In the bifurcation region, it takes time for cells to penetrate or flatten against the ESL and time for such cells to recover from an ESL encounter. In the higher resistivity case, cells penetrate the ESL less and take less time to recover from an ESL encounter. To understand why lower resistivity leads to more penetration, lower resistivity allows for increased circulation in the ESL during a cell-ESL encounter allowing fluid to be more easily displaced as cells flatten or penetrate the ESL. Table 5 confirms the general trend in terms of hydraulic resistivity travel speed with lower hydraulic resistivity simulations experiencing approximately 4 ms greater passage times than higher hydraulic resistivity simulations.

Similar results hold for osmotic pressure differences in the ESL. When only the osmotic pressure difference

is varied, there is no shape disagreement before the bifurcation, as osmotic pressure differences in the ESL have no impact on the governing fluid equations and associated shear rates. After coming into contact with the ESL in the bifurcation, however, there is significant shape disagreement between low and high osmotic pressure difference cases especially in the case of lower hydraulic resistivity (Figure 8c). While shape disagreement peaks immediately after the cells come into contact with the ESL at the bifurcation, note how in Figure 8a the reduction and leveling off of shape disagreement corresponds to a gradual repelling of the RBC from the ESL. This, once again, indicates that greater interaction with the ESL produced by a lower osmotic pressure difference or lower hydraulic resistivity in the ESL can lead to greater shape disagreements between RBCs when the osmotic pressure difference is varied. Lower osmotic pressure difference in the ESL also results in cells that travel faster/farther as they sink into the ESL but slower as they later pull out of the ESL.

4.3 Penetration

Analysis of the deformation results suggest that greater interaction between the ESL and RBCs occurs in scenarios involving lower hydraulic resistivity and osmotic pressure difference values. The interactions tend to lead to decreased deformation and decreased RBC speed. Such interactions are intrinsically tied to the RBC ability to penetrate into the ESL region. Reducing either or both the hydraulic resistivity and osmotic pressure difference in the ESL results in a dramatic increase in an RBC's maximum penetration distance into the ESL (Figure 9a), as well as the length of time an RBC spends impinging upon the ESL (Figure 9b). Lower osmotic pressure differences especially allow the RBC to penetrate more deeply into the ESL (Table 5). At low osmotic pressure differences, the ESL is on average penetrated from 20-52% of its width across the full range of hydraulic resistivities considered here. This is in contrast to high osmotic pressure difference where the ESL is on average penetrated from 2-4% of its width across the same range of hydraulic resistivities. These differences in ESL penetration help explain the effects interaction with the ESL at bifurcations have on RBC deformation and speed.

In general, RBCs are observed to often dramatically reduce velocity when traveling through microvessel bifurcations in what are referred to as "lingering events." Lingering can have such effects as causing the redistribution of following RBCs or breaking up RBC trains (Kihm et al., 2021). This lingering phenomena is also observed in the simulations presented here as cells

slow to less than 30% their original speed when traversing the bifurcation. By interacting more strongly with the ESL, cell speeds are reduced further for lower values of hydraulic resistivity and osmotic pressure difference compared to higher values. Because we are focused here on low hematocrit where interactions rarely occur (because of the choice to start by modeling one cell at a time) and because cells still go relatively quickly through the bifurcation in our scenarios, it is hard to know what the potential impact of lingering cells could be by just using this study. Further study is needed to determine if this additional decrease in speed has a significant effect on lingering dynamics.

4.4 Limitations

Throughout this paper, cell-to-cell interactions have been neglected, corresponding to an approximately zero hematocrit regime. Including cell-cell interactions would help better understand partitioning in bifurcations at nonzero hematocrits. Past results suggest that higher hematocrit levels promote more uniform partitioning (Pries et al., 1989; Barber et al., 2011) but it is not clear how an ESL may affect such trends. In addition, isolated RBCs tend to migrate towards the centerline of the mother vessel, indicating that the distribution upstream of the bifurcation of these RBCs depends on the distance they have traveled. Here, for simplicity, we have assumed a uniform distribution of RBCs upstream of the bifurcation. Considering other upstream distributions may reveal more insights like those seen in Balogh and Bagchi (2018).

Throughout there has been an underlying assumption that we can represent ESL damage to some extent by lowering the hydraulic resistivity and osmotic pressure difference, which corresponds to fewer and/or weaker structural components in the layer. We believe that this assumption provides a reasonable start towards understanding how RBC partitioning, deformation, and penetration may be affected when the ESL is damaged. Nonetheless, ESL damage can be quite complicated and understanding the pathology spectrum more completely may require use of a variable ESL width, alternate representations of flow resistance and ESL rigidity, and auxiliary equations that consider forces between adhesive molecules on the RBCs and ESL.

Here we use a two-dimensional model and while past model validations suggest the model is capable of revealing reasonable insights, a three-dimensional model should be able to reveal further insight. Of particular note is the fact that obstacles tend to obstruct or block flow less in three-dimensions than in two-dimensions, which suggests the obstruction effect and associated

cell-ESL interactions may be diminished in three dimensions. At the same time, it is not immediately clear how cell migration will be affected as cell mechanical properties strongly influence the migration velocity (Losserand et al., 2019). Given cell migration tends to be relatively slow in general, however, we expect that if the vessels considered are small enough and the relative amount of obstruction is near 100%, obstruction will tend to dominate partitioning even in three dimensions. Nonetheless, the vessel diameters at which that happens will likely be smaller than for the two-dimensional case. The effect of obstruction for vessels of the same diameter as those in this study may be diminished in three-dimensions to such an extent that the migration effect becomes dominant, producing the net effect of more uniform partitioning behavior for lowered hydraulic resistivity or osmotic pressure difference. This is especially true as the effect of these parameter changes on partitioning in this two-dimensional study was observed to be relatively minor. A three-dimensional study that considers both cell migration and cell obstruction would best help us understand the full impact of a two vs three-dimensional model. We still expect the mechanisms identified here, however, to still be significant to varying degrees in the three-dimensional setting.

As noted previously, the flux at the daughter vessel outlets is fixed. We chose these boundary conditions (as opposed to prescribing a pressure drop across the bifurcation, for example) for two reasons. The first reason is that the $\Phi(\Psi)$ functions that have been referenced historically rely on an exact prescription for the outgoing flows for both RBCs and total blood flux. The second reason is that there are additional resistances due to additional vessel length and/or networks downstream of the vessel bifurcation. The extent to which the flow in the bifurcation daughter vessels may differ depends on what is going on downstream. For instance, the pressure drop at the mouth of a daughter vessel due to an obstructing cell is approximately 18 dyn/cm². For daughter branch vessels that extend more than 33 microns beyond the obstructing cell without branching into further daughter branches, the relative resistance due to the obstructing RBC is less than 1%. Additional potential networks downstream could further lower that relative resistance. Given capillary path lengths on the order of hundreds of microns are frequently reported in the literature (Zweifach, 1974; Wiedeman, 1962; Batra and Rakusan, 1992; Heiss, 1983), we expect the resistance due to the RBC in such cases will probably be small. Still, as seen in studies that use anatomically based networks (Zakrzewicz et al., 2002; Balogh and Bagchi, 2018; Chang et al., 2017), capillaries can be on

the order of 33 microns and resistance fluctuations can be important including being able to restore partitioning back towards uniformity and to evoke fluctuations between classical and reverse partitioning. Such effects that may be due to resistance fluctuations caused by our RBC can't be detected using our boundary conditions. As such, the possibility of resistance fluctuation effects should be taken into account when interpreting our results. In addition, future studies could try to incorporate such effects by designing pressure outlet conditions that take into account the possibly complicated downstream vessels/network.

RBC partitioning is dependent on the upstream hematocrit distribution. In this study, the upstream cell center positions are assumed to be distributed uniformly. However, the distribution of RBCs *in vivo* depend on additional factors such as the geometry of the vessel network upstream and its effect on cell positions and deformations due to cell migration and cell-cell interactions, among others. A very important related limitation is the assumption of zero hematocrit. While such a simplifying assumption is a useful tool to begin understanding partitioning, in reality cells are rarely alone. This can cause, for instance, fluctuating hematocrit profiles and partitioning behaviors as flow takes place in a given system Balogh and Bagchi (2018). In fact, efforts by Rasmussen et al. (2018) suggest that appropriate use of existing empirical partitioning functions rely on taking into account upstream distributions and their stochasticity. Past applications without taking such matters into account have resulted physiologically unrealistic no-flow vessels. Future work could include consideration of such stochastic upstream distributions in order to better understand how the ESL may, or may not, affect partitioning, typical RBC deformation, and ESL penetration.

For simplicity, the model neglects ESL thickness, irregularity, and adhesivity. A thicker ESL would likely lead to a stronger obstruction effect (more uniform partitioning), while a thinner layer would do the opposite. The effects of ESL structure irregularity are difficult to predict. Large structures at the bifurcation could provide a partial barrier to entrance into one of the vessels while absent structures or holes in the ESL could capture RBCs and subject them to a significantly different partitioning process as well as different ESL-RBC interactions. More studies are needed to investigate the potential effects of ESL irregularity. Cells adhering, as in Vink and Duling (2000), would lead to lingering and higher levels of interaction. Based on Barber et al. (2011), more interaction may encourage more uniform partitioning. The simulations required to say

more about these effects, however, are outside the scope of this study.

The geometry used is one of many possible bifurcations both in terms of vessel arrangement (e.g. branching angle) and vessel size. While some geometric factors are not believed to play a significant role in partitioning (e.g. branching angle (Pries et al., 1989)), others do play a role such as the ratio of the two daughter branch diameters and the mother vessel size. Future studies should investigate these factors and how ESL-cell interactions may depend on such factors.

RBCs are known to be able to squeeze through vessel as small as 2.7 μm in size. In such cases, RBCs undergo much larger deformations than those seen here. If any physiological mechanisms depend solely on the level of RBC deformation, such mechanisms would likely be triggered more often and at greater strength in such small vessels. At the same time, however, there are also spatiotemporal aspects to many physiological mechanisms in the microvasculature. For instance, release of vasodilatory factors upstream of a bifurcation/earlier can yield different flow dynamics in a given vessel network than if such factors are released within the smallest capillaries/later. Such considerations, however, are beyond the scope of this study. Any implications this study might have regarding physiological mechanisms are limited to bifurcations similar in size and shape to the one presented here.

4.5 Summary

In summary, the partitioning, deformation, and ESL penetration of RBCs is affected by the hydraulic resistivity and osmotic pressure difference in the ESL. Increased obstruction effects for increased hydraulic resistivity promote uniform partitioning, but only by a relatively small margin. Increased flow centralization and an increased resistance to compression correspond to increased levels of hydraulic resistivity and osmotic pressure difference, respectively, which usually correlates with increased deformation. An increased resistance to flow and compression also correlates with decreased ESL penetration, which helps explain deformation effects as well as the increased speed at which cells can traverse bifurcations.

Acknowledgements This work has been partially supported by the Department of Mathematics in the School of Science at IUPUI and NSF grant DMS-1522554. We would like to thank Dr. Timothy Secomb (University of Arizona) for suggestions on considering this topic. We would also like to thank Drs. Julia Arciero and Luoding Zhu (IUPUI) and Dr. Peijun Li (Purdue University) for contributing thoughts on this work that partially formed a basis for Dr. Triebold's dissertation.

References

- Balogh P, Bagchi P (2018) Analysis of red blood cell partitioning at bifurcations in simulated microvascular networks. *Physics of Fluids* 30(5):051902, DOI 10.1063/1.5024783
- Barber J, Zhu L (2019) Two-dimensional finite element model of breast cancer cell motion through a microfluidic channel. *Bulletin of Mathematical Biology* pp 1–22, DOI 10.1007/s11538-018-00557-x
- Barber JO (2009) Computational simulation of red blood cell motion in microvascular flows. Doctoral dissertation, University of Arizona
- Barber JO, Alberding JP, Restrepo JM, Secomb TW (2008) Simulated two-dimensional red blood cell motion, deformation, and partitioning in microvessel bifurcations. *Annals of Biomedical Engineering* 36(10):1690–1698, DOI 10.1007/s10439-008-9546-4
- Barber JO, Restrepo JM, Secomb TW (2011) Simulated red blood cell motion in microvessel bifurcations: Effects of cell-cell interactions on cell partitioning. *Cardiovasc Eng Technol* 2(4):349–360, DOI 10.1007/s13239-011-0064-4
- Batra S, Rakusan K (1992) Capillary length, tortuosity, and spacing in rat myocardium during cardiac cycle. *American Journal of Physiology-Heart and Circulatory Physiology* 263(5):H1369–H1376
- Bor-Kucukatay M, Wenby RB, Meiselman HJ, Baskurt OK (2003) Effects of nitric oxide on red blood cell deformability. *American Journal of Physiology-Heart and Circulatory Physiology* 284(5):H1577–H1584, DOI 10.1152/ajpheart.00665.2002
- Brinkman HC (1947) A calculation of the viscous force exerted by a flowing fluid on a dense swarm of particles. *Journal of Applied Sciences Research* A1:27–34
- Chang SS, Tu S, Baek KI, Pietersen A, Liu YH, Savage VM, Hwang SPL, Hsiai TK, Roper M (2017) Optimal occlusion uniformly partitions red blood cells fluxes within a microvascular network. *PLoS computational biology* 13(12):e1005892
- Curry FRE, Arkill KP, Michel CC (2020) The functions of endothelial glycocalyx and their effects on patient outcomes during the perioperative period: A review of current methods to evaluate structure-function relations in the glycocalyx in both basic research and clinical settings. *Perioperative fluid management* pp 75–118
- Damiano E (1998) The effect of the endothelial-cell glycocalyx on the motion of red blood cells through capillaries. *Microvascular Research* 55(1):77–91, DOI <https://doi.org/10.1006/mvres.1997.2052>
- Desjardins C, Duling BR (1990) Heparinase treatment suggests a role for the endothelial cell glycocalyx in regulation of capillary hematocrit. *American Journal of Physiology-Heart and Circulatory Physiology* 258(3):H647–H654
- Evans EA, Skalak R (1979) Mechanics and thermodynamics of biomembranes: part 2. *CRC Crit Rev Bioeng* 3(4):331–418
- Fedosov DA, Caswell B, Suresh S, Karniadakis GE (2011) Quantifying the biophysical characteristics of plasmodium-falciparum-parasitized red blood cells in microcirculation. *Proc Natl Acad Sci U S A* 108(1):35–9, DOI 10.1073/pnas.1009492108
- Forsyth AM, Wan J, Owrutsky PD, Abkarian M, Stone HA (2011) Multiscale approach to link red blood cell dynamics, shear viscosity, and atp release. *Proceedings of the National Academy of Sciences* 108(27):10986–10991, DOI 10.1073/pnas.1101315108
- Forsyth AM, Braummuller S, Wan J, Franke T, Stone HA (2012) The effects of membrane cholesterol and simvastatin on red blood cell deformability and atp release. *Microvasc Res* 83(3):347–51, DOI 10.1016/j.mvr.2012.02.004
- Fu BM, Tarbell JM (2013) Mechano-sensing and transduction by endothelial surface glycocalyx: composition, structure, and function. *Wiley Interdiscip Rev Syst Biol Med* 5(3):381–90, DOI 10.1002/wsbm.1211
- Fung YC (1973) Stochastic flow in capillary blood vessels. *Microvascular research* 5(1):34–48
- Hariprasad DS, Secomb TW (2012) Motion of red blood cells near microvessel walls: effects of a porous wall layer. *J Fluid Mech* 705:195–212, DOI 10.1017/jfm.2012.102
- Heinrich V, Ritchie K, Mohandas N, Evans E (2001) Elastic thickness compressibility of the red cell membrane. *Biophys J* 81(3):1452–63, DOI 10.1016/s0006-3495(01)75800-6
- Heiss H (1983) *Human physiology*. edited by robert f. schmidt and gerhard thews. springer-verlag, berlin-heidelberg-new york (1983) 725 pages, 569 figures, approx. 39.20 isbn: 3-540-11669-9
- Kihm A, Quint S, Laschke MW, Menger MD, John T, Kaestner L, Wagner C (2021) Lingering dynamics in microvascular blood flow. *Biophysical Journal* 120(3):432–439
- Kimura H, Braun RD, Ong ET, Hsu R, Secomb TW, Papahadjopoulos D, Hong K, Dewhirst MW (1996) Fluctuations in red cell flux in tumor microvessels can lead to transient hypoxia and reoxygenation in tumor parenchyma. *Cancer Res* 56(23):5522–8
- Lee DH, Dane MJ, van den Berg BM, Boels MG, van Teeffelen JW, de Mutsert R, den Heijer M, Rosendaal FR, van der Vlag J, van Zonneveld AJ, Vink H, Rabelink TJ, group NEOs (2014) Deeper penetration of erythrocytes into the endothelial glycocalyx is asso-

- ciated with impaired microvascular perfusion. *PLoS One* 9(5):e96477, DOI 10.1371/journal.pone.0096477
- Levick JR (2004) Revision of the starling principle: new views of tissue fluid balance. *The Journal of Physiology* 557(3):704–704, DOI <https://doi.org/10.1113/jphysiol.2004.066118>
- Li X, Popel AS, Karniadakis GE (2012) Blood–plasma separation in y-shaped bifurcating microfluidic channels: a dissipative particle dynamics simulation study. *Physical biology* 9(2):026010
- Losserland S, Coupier G, Podgorski T (2019) Migration velocity of red blood cells in microchannels. *Microvascular research* 124:30–36
- Lücker A, Weber B, Jenny P (2015) A dynamic model of oxygen transport from capillaries to tissue with moving red blood cells. *American Journal of Physiology-Heart and Circulatory Physiology* 308(3):H206–H216
- Mantegazza A, Clavica F, Obrist D (2020a) In vitro investigations of red blood cell phase separation in a complex microchannel network. *Biomicrofluidics* 14(1):014101
- Mantegazza A, Ungari M, Clavica F, Obrist D (2020b) Local versus global blood flow modulation in artificial microvascular networks: effects on red blood cell distribution and partitioning. *Frontiers in physiology* 11:1117
- Mayrovitz HN, Roy J (1983) Microvascular blood flow: evidence indicating a cubic dependence on arteriolar diameter. *Am J Physiol* 245(6):H1031–8, DOI 10.1152/ajpheart.1983.245.6.H1031
- Mulivor AW, Lipowsky HH (2002) Role of glycocalyx in leukocyte-endothelial cell adhesion. *Am J Physiol Heart Circ Physiol* 283(4):H1282–91, DOI 10.1152/ajpheart.00117.2002
- Oberleithner H (2013) Vascular endothelium leaves fingerprints on the surface of erythrocytes. *Pflügers Archiv : European journal of physiology* 465, DOI 10.1007/s00424-013-1288-y
- Oberleithner H, Wälte M, Kusche-Vihrog K (2015) Sodium renders endothelial cells sticky for red blood cells. *Frontiers in physiology* 6:188, DOI 10.3389/fphys.2015.00188
- Obrist D, Weber B, Buck A, Jenny P (2010) Red blood cell distribution in simplified capillary networks. *Philosophical Transactions of the Royal Society A: Mathematical, Physical and Engineering Sciences* 368(1921):2897–2918
- PDE Solutions Inc (2021) Flexpde version 7.17. URL <http://www.pdesolutions.com>
- Pfafferoth C, Nash GB, Meiselman HJ (1985) Red blood cell deformation in shear flow. effects of internal and external phase viscosity and of in vivo aging. *Biophys J* 47(5):695–704, DOI 10.1016/S0006-3495(85)83966-7
- Pries A, Ley K, Claassen M, Gaehtgens P (1989) Red cell distribution at microvascular bifurcations. *Microvascular research* 38(1):81–101
- Pries AR, Secomb TW (2005) Microvascular blood viscosity in vivo and the endothelial surface layer. *Am J Physiol Heart Circ Physiol* 289(6):H2657–64, DOI 10.1152/ajpheart.00297.2005
- Pries AR, Secomb TW (2008) Blood flow in microvascular networks. In: *Microcirculation*, Elsevier, pp 3–36
- Pries AR, Secomb TW, Gaehtgens P, Gross JF (1990) Blood flow in microvascular networks. experiments and simulation. *Circulation Research* 67(4):826–834, DOI 10.1161/01.RES.67.4.826
- Pries AR, Secomb TW, Gessner T, Sperandio MB, Gross JF, Gaehtgens P (1994) Resistance to blood flow in microvessels in vivo. *Circ Res* 75(5):904–15, DOI 10.1161/01.res.75.5.904
- Pries AR, Secomb TW, Jacobs H, Sperandio M, Osterloh K, Gaehtgens P (1997) Microvascular blood flow resistance: role of endothelial surface layer. *Am J Physiol* 273(5):H2272–9, DOI 10.1152/ajpheart.1997.273.5.H2272
- Pries AR, Secomb TW, Sperandio M, Gaehtgens P (1998) Blood flow resistance during hemodilution: effect of plasma composition. *Cardiovasc Res* 37(1):225–35, DOI 10.1016/s0008-6363(97)00226-5
- Pries AR, Secomb TW, Gaehtgens P (2000) The endothelial surface layer. *Pflügers Arch* 440(5):653–66, DOI 10.1007/s004240000307
- Pskowski A, Bagchi P, Zahn JD (2021) Investigation of red blood cell partitioning in an in vitro microvascular bifurcation. *Artificial Organs*
- Rasmussen PM, Secomb TW, Pries AR (2018) Modeling the hematocrit distribution in microcirculatory networks: a quantitative evaluation of a phase separation model. *Microcirculation* 25(3):e12445
- Rostgaard J, Qvortrup K (1997) Electron microscopic demonstrations of filamentous molecular sieve plugs in capillary fenestrae. *Microvascular Research* 53(1):1–13, DOI <https://doi.org/10.1006/mvre.1996.1987>
- Schmid-Schonbein GW, Skalak R, Usami S, Chien S (1980) Cell distribution in capillary networks. *Microvasc Res* 19(1):18–44, DOI 10.1016/0026-2862(80)90082-5
- Secomb T, Pries A (2013) Blood viscosity in microvessels: experiment and theory. *Comptes rendus Physique* 14 6:470–478
- Secomb TW, Hsu R, Pries AR (1998) A model for red blood cell motion in glycocalyx-lined capillaries. *Am J Physiol* 274(3):H1016–22, DOI 10.1152/ajpheart.1998.274.3.H1016

- Secomb TW, Hsu R, Pries AR (2001) Effect of the endothelial surface layer on transmission of fluid shear stress to endothelial cells. *Biorheology* 38(2-3):143–50
- Secomb TW, Hsu R, Pries AR (2002) Blood flow and red blood cell deformation in nonuniform capillaries: effects of the endothelial surface layer. *Microcirculation* 9(3):189–96, DOI 10.1038/sj.mn.7800132
- Secomb TW, Styp-Rekowska B, Pries AR (2007) Two-dimensional simulation of red blood cell deformation and lateral migration in microvessels. *Annals of Biomedical Engineering* 35(5):755–765, DOI 10.1007/s10439-007-9275-0
- Squire JM, Chew M, Nneji G, Neal C, Barry J, Michel C (2001) Quasi-periodic substructure in the microvessel endothelial glycocalyx: A possible explanation for molecular filtering? *Journal of Structural Biology* 136(3):239–255, DOI <https://doi.org/10.1006/jsbi.2002.4441>
- Svanes K, Zweifach B (1968) Variations in small blood vessel hematocrits produced in hypothermic rats by micro-occlusion. *Microvascular Research* 1(2):210–220
- Vink H, Duling BR (1996) Identification of distinct luminal domains for macromolecules, erythrocytes, and leukocytes within mammalian capillaries. *Circ Res* 79(3):581–9, DOI 10.1161/01.res.79.3.581
- Vink H, Duling BR (2000) Capillary endothelial surface layer selectively reduces plasma solute distribution volume. *Am J Physiol Heart Circ Physiol* 278(1):H285–9, DOI 10.1152/ajpheart.2000.278.1.H285
- Vink H, Constantinescu AA, Spaan JA (2000) Oxidized lipoproteins degrade the endothelial surface layer : implications for platelet-endothelial cell adhesion. *Circulation* 101(13):1500–2, DOI 10.1161/01.cir.101.13.1500
- Weinbaum S, Tarbell JM, Damiano ER (2007) The structure and function of the endothelial glycocalyx layer. *Annual Review of Biomedical Engineering* 9(1):121–167, DOI 10.1146/annurev.bioeng.9.060906.151959
- Weisel JW, Litvinov RI (2019) Red blood cells: the forgotten player in hemostasis and thrombosis. *J Thromb Haemost* 17(2):271–282, DOI 10.1111/jth.14360
- Wiedeman MP (1962) Lengths and diameters of peripheral arterial vessels in the living animal. *Circulation research* 10(4):686–690
- Williams TN, Thein SL (2018) Sick cell anemia and its phenotypes. *Annu Rev Genomics Hum Genet* 19:113–147, DOI 10.1146/annurev-genom-083117-021320
- Ye T, Peng L, Li G (2019) Red blood cell distribution in a microvascular network with successive bifurcations. *Biomechanics and modeling in mechanobiology* 18(6):1821–1835
- Yedgar S, Kaul DK, Barshtein G (2008) Rbc adhesion to vascular endothelial cells: more potent than rbc aggregation in inducing circulatory disorders. *Microcirculation* 15(7):581–583
- Yen WY, Cai B, Zeng M, Tarbell JM, Fu BM (2012) Quantification of the endothelial surface glycocalyx on rat and mouse blood vessels. *Microvasc Res* 83(3):337–46, DOI 10.1016/j.mvr.2012.02.005
- Zakrzewicz A, Secomb TW, Pries AR (2002) Angioadaptation: keeping the vascular system in shape. *Physiology* 17(5):197–201
- Zhang H, Shen Z, Hogan B, Barakat AI, Misbah C (2018) Atp release by red blood cells under flow: Model and simulations. *Biophys J* 115(11):2218–2229, DOI 10.1016/j.bpj.2018.09.033
- Zhao E, Barber J, Burch M, Unthank J, Arciero J (2020) Modeling acute blood flow responses to a major arterial occlusion. *Microcirculation* 27(4):e12610, DOI 10.1111/micc.12610
- Zweifach BW (1974) Quantitative studies of microcirculatory structure and function: I. analysis of pressure distribution in the terminal vascular bed in cat mesentery. *Circulation Research* 34(6):841–857